frontiers | Frontiers in Earth Science

TYPE Original Research
PUBLISHED 22 January 2025
DOI 10.3389/feart.2024.1514658

OPEN ACCESS

EDITED BY
Hossein Azizi,
University of Kurdistan, Iran

REVIEWED BY
Liang Qiu,
China University of Geosciences, China
Abdolnaser Fazlnia,
Urmia University, Iran

*CORRESPONDENCE
Chenglu Li,
✉ LCL230881@163.com

RECEIVED 21 October 2024
ACCEPTED 12 December 2024
PUBLISHED 22 January 2025

CITATION
Lu S, Li C, Alam M, Song Z, Zhu X, Fu A and Yang W (2025) Geochronology and geochemistry of the Neoproterozoic–Mesozoic intrusive rocks in the Xinlin area, northeastern China: new constraints on the tectonic evolution of the Erguna block.
Front. Earth Sci. 12:1514658.
doi: 10.3389/feart.2024.1514658

Geochronology and geochemistry of the Neoproterozoic–Mesozoic intrusive rocks in the Xinlin area, northeastern China: new constraints on the tectonic evolution of the Erguna block

Sheng Lu[1,2,3,4], Chenglu Li[1]*, Masroor Alam[5], Zhichao Song[4], Xiannan Zhu[3], Anzong Fu[1] and Wenpeng Yang[1]

[1]Natural Resources Survey Institute of Heilongjiang Province, Heilongjiang Provincial Bureau of Geology and Mineral Resources, Harbin, China, [2]MNR Key Laboratory of Metallogeny and Mineral Assessment, Institute of Mineral Resources, Chines Academy of Geological Sciences, Beijing, China, [3]Harbin Center for Integrated Natural Resources Survey, Chines Academy of Geological Sciences, Observation and Research Station of Earth Critical Zone in Black Soil, Ministry of Natural Resources, Harbin, China, [4]The Fifth Geological Exploration Institute of Heilongjiang Province, Heilongjiang Provincial Bureau of Geology and Mineral Resources, Harbin, China, [5]Department of Earth Sciences, Karakoram International University, Gilgit, Pakistan

The occurrence of intrusive rocks within the Xinlin area, northeastern China, provides insights into the Neoproterozoic–Mesozoic geodynamic setting of the Erguna block. In this study, we present petrographic, geochemical, and geochronological data on intrusive rocks from the Xinlin area. Zircon U–Pb and muscovite $^{40}Ar/^{39}Ar$ geochronology reveal that magmatism occurred during the Neoproterozoic (ca. 864.98 Ma), Early Ordovician (ca. 470.0 Ma), Late Carboniferous (ca. 306.9 Ma), Early Permian (ca. 296.9 Ma), and Early Cretaceous (ca. 117.8 Ma) periods. The Neoproterozoic and Early Ordovician intermediate–mafic intrusive rocks have low Rb/Sr contents, high $Mg^{\#}$, and weakly negative Eu anomalies. These results suggest that the magma sources of these rocks varied: intermediate–acidic magmas were derived from the lower crust, and intermediate–mafic magmas originated from the mantle and were subsequently contaminated by crustal material. In contrast, the Late Carboniferous, Early Permian, Late Triassic–Early Jurassic, and Early Cretaceous intermediate–acidic intrusive rocks display high Rb/Sr contents, low $Mg^{\#}$, and strongly negative Eu anomalies, indicating derivation from the partial melting of the lower crust. Our findings, along with previous studies, suggest that Neoproterozoic intrusive rocks were formed during the breakup of the Rodinia supercontinent. The Paleozoic intrusive rocks are associated with the collision and amalgamation of the Erguna and Xing'an blocks, as well as the Songnen and Xing'an blocks. Early Mesozoic intrusive rocks were developed during the subduction of the Mongol-Okhotsk oceanic intracontinental system. Finally, the late Mesozoic intrusive rocks were formed in a non-orogenic extensional setting, potentially linked to the final closure of the Mongol-Okhotsk Ocean or the rollback of the Paleo-Pacific Plate.

KEYWORDS

LA-ICP-MS zircon U–Pb dating, intrusive rock, Xinlin area, muscovite 40Ar/39Ar dating, geochemistry

1 Introduction

The Great Xing'an Range is located within the suture zone between the Siberian and North China cratons (Figure 1A; Liu et al., 2017). This area records evidence of several tectonic events, including the convergence and breakup of the Rodinia supercontinent during the Proterozoic (Zhao, 2017), the closure of the Paleo-Asian Ocean during the late Paleozoic, the closure of the Mongol-Okhotsk Ocean (MOO) in the late Mesozoic, and the subduction of Paleo-Pacific oceanic plate since the Jurassic (Xu et al., 2013). The tectonic setting and geochemical characteristics of the magmatic rocks in this area are notably complex, featuring diverse rock types. Consequently, the region has garnered significant interest from geologists both domestically and internationally (Jia et al., 2011; Liu et al., 2011; Ge et al., 2015; Ouyang et al., 2015; Zheng., 2015).

The Xinlin area, located in the Erguna block, is an important gold-mining district (Figure 1B; Liu et al., 2017). The area hosts well-developed intrusive rocks, primarily comprising Neoproterozoic, Paleozoic, and Mesozoic formations (Figure 1C). Extensive research has been conducted on the chronology, geochemistry, and tectonic framework of the magmatic rocks in this area (Wu et al., 2009; Wang et al., 2012; Shi et al., 2013; Feng, 2015; Liu et al., 2016; Tang, 2016; Zhao, 2017; Qian et al., 2018; Liu et al., 2021). However, debates persist regarding the tectonic setting and origin of the Neoproterozoic–Mesozoic intrusive rocks in the Erguna block.

In this study, we present new petrographic, geochemical, and geochronological data on the different types of intrusive rocks within the Xinlin area. We discuss their petrogenesis and reconstruct the tectonic evolution of the region from the Neoproterozoic to the Mesozoic periods.

2 Geological background

The strata exposed in the study area include the Neoproterozoic Xinghuadukou Group; the Lower Cambrian Hongshenggou, Sanyigou, and Jiaobuleshihe formations; the Lower Ordovician Kunasenhe, Huangbanji, and Daxiyikanghe formations; the Lower–Middle Ordovician Tongshan and Duobaoshan formations; the Upper Ordovician Anniangniangqiao and Aihui formations; the Lower Silurian Huanghuagou Formation; the Upper Silurian to Middle Devonian Niqiuhe Formation; and the Lower Cretaceous Longjiang, Guanghua, and Ganhe formations (Figure 1C; HBGMR, 1997).

Intrusive rocks are well-developed in the study area, and they primarily include Neoproterozoic, Paleozoic, and Mesozoic intrusive rocks (Figure 1C). The Neoproterozoic magmatic rocks are mainly distributed in the northern part of Walali, with lithologies predominantly comprising gneiss and schist. The Paleozoic intrusive rocks exposed in the study area are mainly Hercynian and Indosinian in origin. Mesozoic intrusive rocks can be divided into early Yanshanian and late Yanshanian phases. The early Yanshanian intrusive rocks are mainly distributed in the northwest of the study area, with lithologies mainly consisting of monzonitic granite and syenite granite, which are dated to the late Triassic–early Jurassic. The late Yanshanian magmatic rocks are less exposed and show scattered distribution characteristics across the study area, with lithologies primarily comprising granite veins and diorite veins. The majority of the faults within the study area are normal or strike-slip faults, predominantly trending NW–SE and NE–SW, with some trending N–S and E–W. These faults are interpreted to have formed in an extensional setting (Shao and Mu, 1999; Figure 1C).

2.1 Petrology

2.1.1 Neoproterozoic intrusive rocks

The Neoproterozoic intrusive rocks outcrop in the northern part of Walali within the study area. These rocks have undergone regional metamorphism. The dominant lithology is hornblende gneiss (Figure 1C). The hornblende gneisses are gray–black, exhibit a sheet-like, columnar, granular, crystalloblastic structure, and are primarily composed of plagioclase (50 vol.%), quartz (25 vol.%), biotite (20 vol.%), and amphibole (5 vol.%) (Figures 2A, B).

2.1.2 Paleozoic intrusive rocks

Paleozoic intrusive rocks primarily include Early Ordovician, Late Carboniferous, and Early Permian intrusive rocks in the study area. The Early Ordovician intrusive rocks mainly outcrop in the Beixili region of the study area. The predominant lithology is gabbro (Figure 1C). The gabbros are gray–black, display a cataclastic structure, and are mainly composed of plagioclase (70 vol.%), pyroxene (15 vol.%), biotite (10 vol.%), and hornblende (5 vol.%) (Figures 2C,D). The Late Carboniferous intrusive rocks outcrop mainly near the Walali gold deposit. The dominant lithologies are monzonitic granite (Figures 2E,F) and potash feldspar granite (Figures 2G,H). The Early Permian intrusive rocks extensively outcrop in the northeastern part of the study area. The lithologies are mainly monzonitic granite and syenogranite.

2.1.3 Early Cretaceous intrusive rocks

Mesozoic intrusive rocks primarily include Late Triassic–Early Jurassic and Early Cretaceous rocks in the study area. The Late Triassic–Early Jurassic intrusive rocks are widely exposed

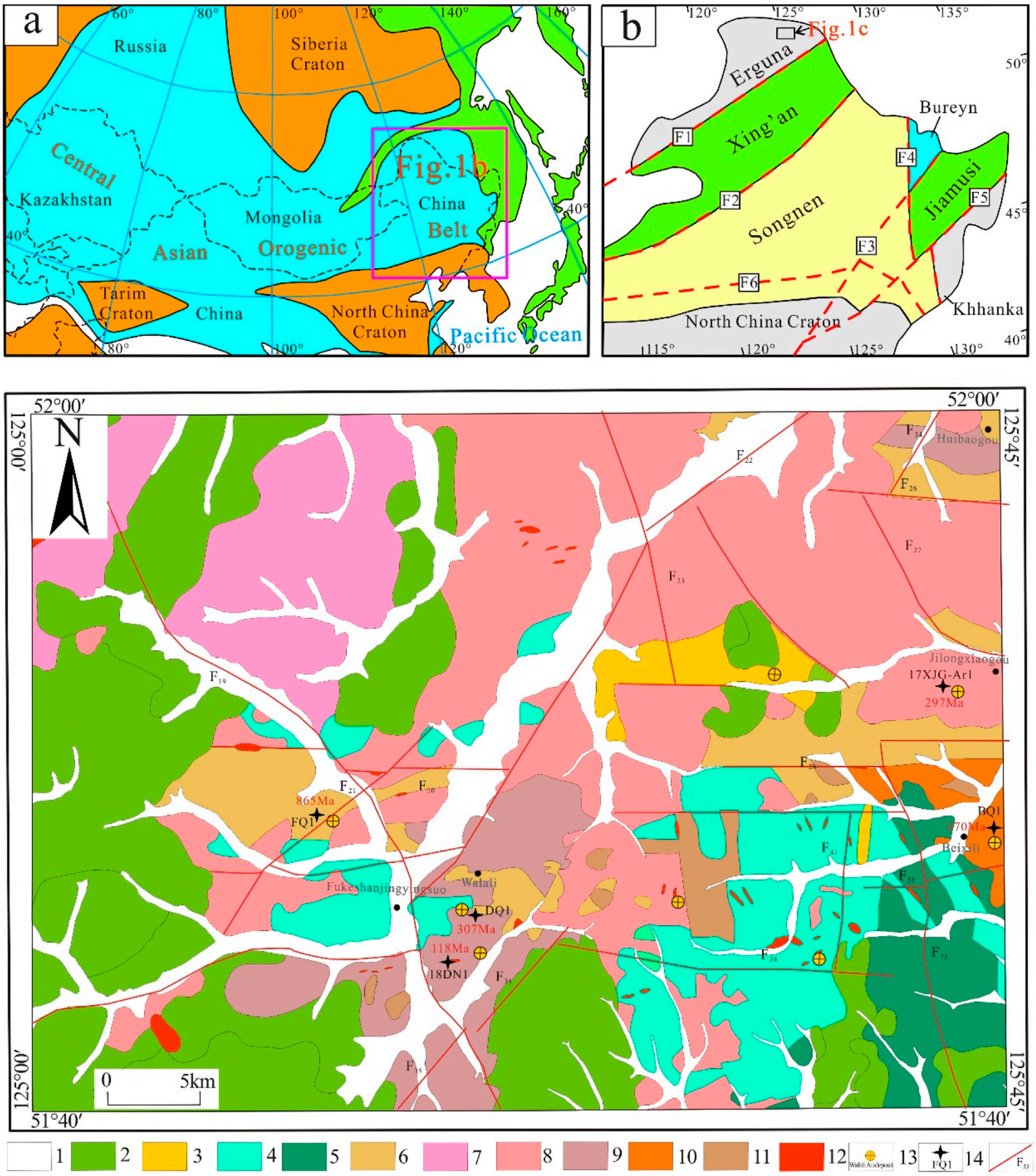

FIGURE 1
(A) Location of the study area in the Central Asian Orogenic Belt (modified after Jahn, 2004). **(B)** Tectonic map of the Great Xing'an Range, showing its structures and tectonic belts (modified after Liu et al., 2017). **(C)** Geological map of the study area showing sampling locations. 1, Quaternary; 2, Early Cretaceous volcanic rocks; 3, Silurian–Devonian strata; 4, Ordovician strata; 5, Cambrian strata; 6, Neoproterozoic Xinghuadukou rock group; 7, Late Triassic–Early Jurassic intrusive rocks; 8, Early Permian intrusive rocks; 9, Late Carboniferous intrusive rocks; 10, Early Ordovician intrusive rocks; 11, Neoproterozoic intrusive rocks; 12, vein rock; 13, Au deposit location and number; 14, sample location and number; 15, fault, including fault number.

in the northwestern part of the study area. The predominant lithologies are monzonitic granite (Figures 2I,J) and syenogranite. The Early Cretaceous intrusive rocks occur as scattered small exposures resembling "rock trees" across the study area. The dominant lithologies are granite and diorite veins (Figures 2K,L).

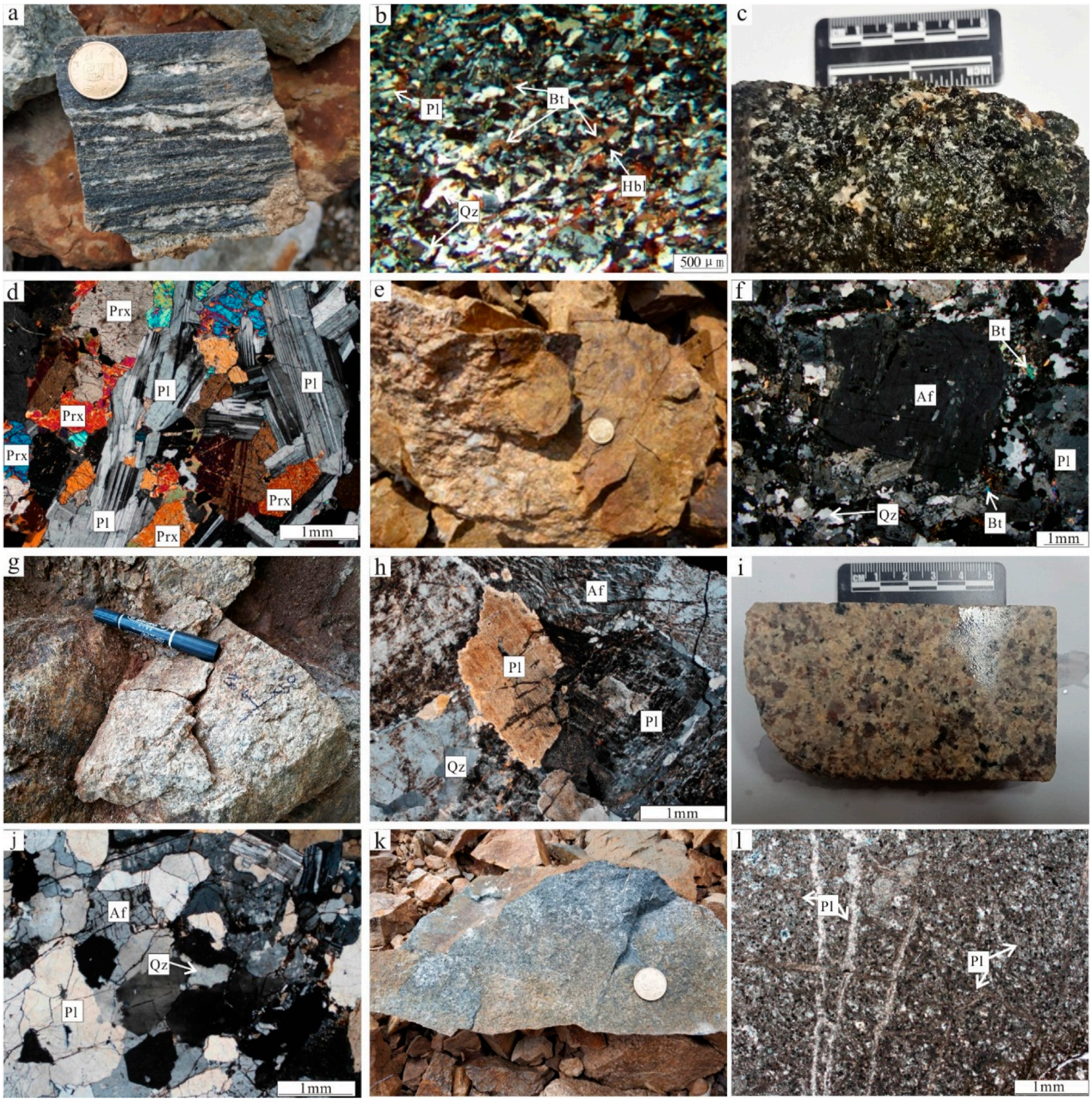

FIGURE 2
Photomicrographs and field photographs of intrusive rocks in the study area. **(A)** Hornblende gneisses; **(B)** hornblende gneisses (+); **(C)** gabbro; **(D)** gabbro (+); **(E)** monzonitic granite; **(F)** monzonitic granite (+); **(G)** potash feldspar granite; **(H)** potash feldspar granite (+); **(I)** monzonitic granite; **(J)** monzonitic granite (+); **(K)** diorite; **(L)** diorite (+). Af, alkali feldspar; Pl, plagioclase; Qz, quartz; Hb, hornblende; Bt, biotite; Prx,pyroxene.

3 Sample collection and analytical methods

3.1 Sample collection

Four rock samples were collected for zircon U–Pb geochronology, with rock types including hornblende gneiss (FQ1), gabbro (BQ1), monzonitic granite (DQ1), and diorite (18DN1). One sample was collected for muscovite Ar–Ar geochronology (sample 17XJG-Ar_1). Twenty-seven samples were collected for whole-rock geochemical analyses, with rock types including six hornblende gneisses (samples FQ1, FQ2, FQ4, FQ5, FQ7, and FQ8), five gabbros (samples BQ1, BQ2, BQ3, BQ4, and BQ5), eight monzonitic granites (samples DQ1, DQ2, DQ3, P_{60}GS3, GS1179, GS4075, P_{54}GS1, and P_{52}GS30), three potash feldspar granites (samples WQ15, WQ16, and WQ17), three syenogranites (samples P52GS3, GS4071, and GS 2065), one alkali feldspar granite (sample P_{50}GS9), and one diorite (sample P_{63}GS6).

3.2 Analytical methods

The zircon grains were separated from the crushed samples by using conventional heavy liquid and magnetic techniques, and cathodoluminescence (CL) imaging and zircon U–Pb dating were conducted at the Beijing Createch Testing Technology, Beijing, China. The ICPMSDataCal (version 9.9; Liu et al., 2010) and Isoplot (version 3.0; Ludwig, 2003) programs were used for data reduction. Common Pb was corrected following the method outlined by Andersen (2002). Analytical uncertainties are reported at the 95% (2σ) confidence level.

The muscovite samples were collected from granite closely associated with mineralization. The correction factors used for interfering argon isotopes derived from Ca and K were $(^{39}Ar/^{37}Ar)_{Ca} = 8.06 \times 10^{-4}$, $(^{36}Ar/^{37}Ar)_{Ca} = 2.389 \times 10^{-4}$, and $(^{40}Ar/^{39}Ar)_{K} = 5.872 \times 10^{-3}$. ^{37}Ar was corrected for radioactive decay, and the ^{40}K decay constant is $\lambda = 5.543 \times 10^{-10} a^{-1}$ (Steiger and Jager, 1977). The plateau age and the positive and negative isochrones (Ludwig, v2.49) were calculated using the Isoplot program, with the plateau age errors reported at 2 σ. The analytical procedures followed those outlined by Zhang et al. (2006) and Chen et al. (2006).

Major and trace-element analyses were conducted at the Institute of Regional Geology and Mineral Resources, Hebei Province, China. The major elements were analyzed using X-ray fluorescence (XRF), with accuracy better than 5%, and the trace elements were analyzed by inductively coupled plasma–mass spectrometry (ICP–MS), with accuracy better than 10%.

4 Analytical results

4.1 Zircon U–Pb geochronology

Zircons from hornblende gneiss (sample FQ1) are predominantly rounded, with some displaying long columnar shapes (Figure 3A). The U and Th contents of hornblende gneiss (sample FQ1) range from 142.86 to 452.90 ppm and 302.48 to 650.35 ppm, respectively, with Th/U ratios of 0.39–0.72 (n = 17; Table 1), which is consistent with a magmatic origin. Analyses yield $^{206}Pb/^{238}U$ ages of 839–883 Ma with a weighted-mean age of 864.9 ± 5.4 Ma (MSWD = 1.02) (Figure 3B).

Zircons from gabbro (sample BQ1) are primarily rounded, with some exhibiting columnar shapes (Figure 3C). The U and Th contents of gabbro (sample BQ1) range from 1,020.27 to 10,980.61 ppm and 6,553.42 to 42,051.31 ppm, respectively, with Th/U ratios of 0.13–0.29 (n = 19; Table 1), which is consistent with a magmatic origin. Analyses yield $^{206}Pb/^{238}U$ ages of 458–480 Ma with a weighted-mean age of 470.0 ± 2.9 Ma (MSWD = 0.90) (Figure 3D).

Zircons from monzonitic granite (sample DQ1) exhibit well-developed crystals, bright cathodoluminescence, complete growth rings, and pronounced rhythmic zoning (Figure 3E). The U and Th contents range from 42.21 to 572.40 ppm and 92.40 to 521.29 ppm, respectively, with Th/U ratios of 0.86–2.19 (n = 17; Table 1), suggesting a magmatic origin. Analyses yield $^{206}Pb/^{238}U$ ages of 304–309 Ma with a weighted-mean age of 306.9 ± 1.9 Ma (MSWD = 0.14) (Figure 3F).

Zircons of diorite (sample 18DN1) are well-crystallized with flattened shapes (Figure 3G). The U and Th contents range from 205.55 to 885.81 ppm and 257.12 to 788.38 ppm, respectively, with Th/U ratios of 0.74–1.28 (n = 10; Table 1), indicative of a magmatic origin. Analyses yield $^{206}Pb/^{238}U$ ages of 113–124 Ma with a weighted-mean age of 117.8 ± 3.1 Ma (MSWD = 2.0) (Figure 3H).

4.2 Muscovite $^{40}Ar/^{39}Ar$ dating

The Ar–Ar dating results of muscovite are presented in Table 2. The corresponding plateau age, isochron age (Figure 4A), and inverse isochron age are illustrated in Figure 4B. The muscovite sample yielded an $^{40}Ar/^{39}Ar$ plateau age of 296.9 ± 1.7 Ma (nine-step age-heating spectrum from 850°C to 1,300°C, and 87.9% of ^{39}Ar released), a corresponding isochron age of 300.3 ± 1.7 Ma (950°C–1,200°C, N = 8, MSWD = 3.2), and an inverse isochron age of 299.9 ± 1.7 Ma (950°C–1,200°C, N = 8, MSWD = 3.7). These data indicate that the plateau age (296.9 ± 1.7 Ma) represents the reliable crystallization age of the muscovite.

4.3 Geochemistry

The Neoproterozoic hornblende gneisses belong to the calc-alkaline series and exhibit high total alkali contents (Table 3). The samples mainly plot within the monzonite field on the TAS diagram (Figure 5A). In the K_2O–SiO_2 diagram, they fall within the high-K calc-alkaline series and are peraluminous (Figure 5C). The Neoproterozoic hornblende gneisses yielded Eu/Eu^*values of 0.62–0.82 and $(La/Yb)_N$ values ranging from 5.30 to 30.62. Rare earth element (REE) fractionation is minimal. The chondrite-normalized REE diagram (Figure 6A) indicates a slight enrichment of light rare earth elements (LREEs) with a subtle positive trend. The primitive-mantle-normalized trace-element spider diagram (Figure 6B) shows enrichment in large-ion lithophile elements (LILEs; e.g., Rb, Ba, Th, U, La, Nd, and Ce) and depletion in high-field-strength elements (HFSEs; e.g., Ta, P, and Nb; Table 3).

The Early Ordovician gabbro rocks are characterized by low Si and high Mg contents (Table 3). These samples primarily plot near the gabbro field on the TAS diagram (Figure 5A). They exhibit Eu/Eu^*values ranging from 0.85 to 2.16 and $(La/Yb)_N$ values of 1.10–3.94, with significant REE fractionation. The chondrite-normalized REE diagram (Figure 6C) shows enrichment in LREEs, exhibiting a positive trend. The primitive-mantle-normalized trace-element spider diagram (Figure 6D) indicates enrichment in LILEs (e.g., Rb, Sr, and Ba) and depletion in HFSEs (e.g., Zr, Hf, and P; Table 3).

The Late Carboniferous, Early Permian, Late Triassic–Early Jurassic, and Early Cretaceous intrusive rocks belong to the calc-alkaline series, with high total alkali contents (Table 3). These samples fall in the field of high-K calc-alkaline series on the K_2O–SiO_2 diagram (Figure 5B) and are peraluminous

10.3389/feart.2024.1514658

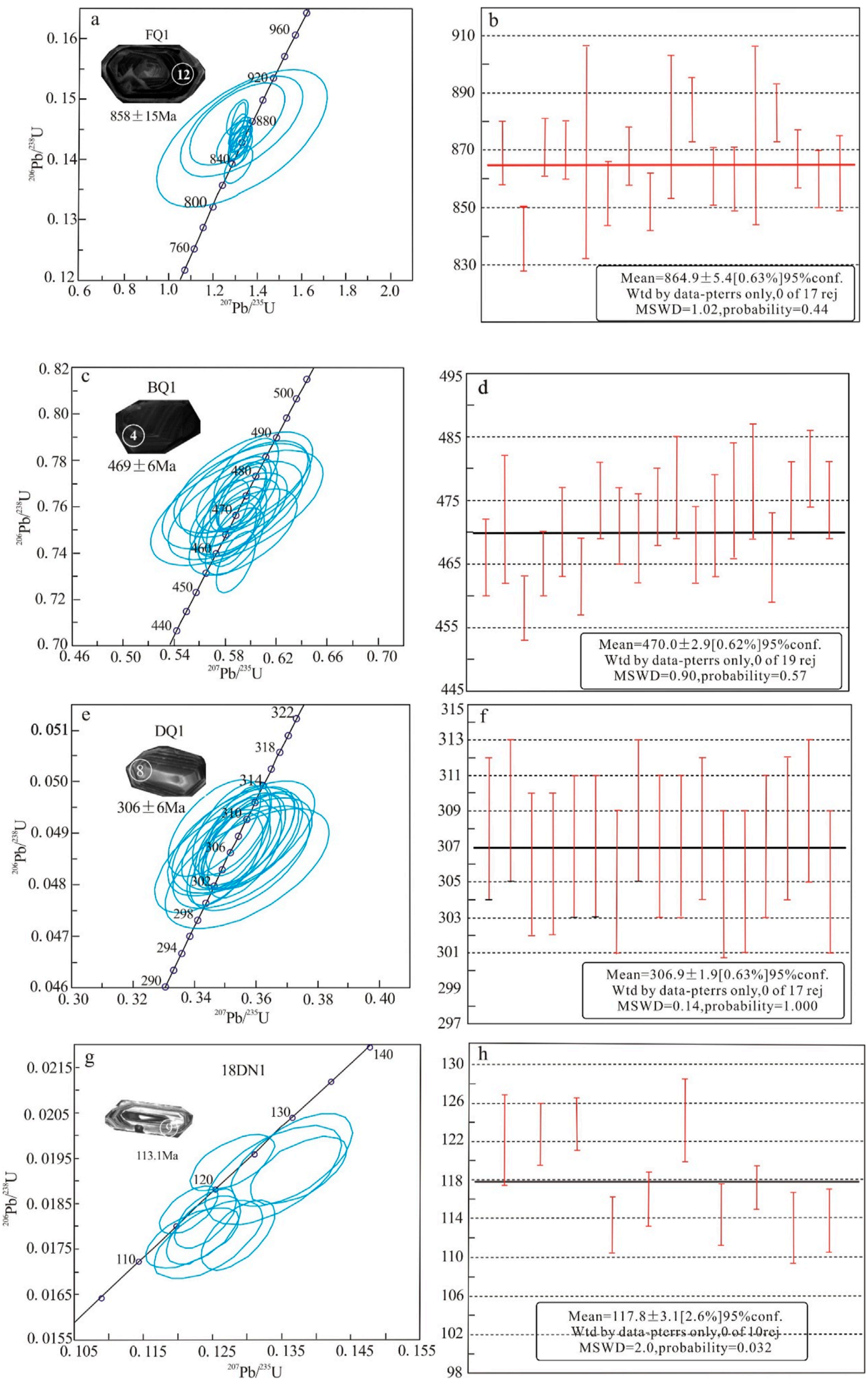

FIGURE 3
Zircon harmonic age map **(A, C, E, and G)** and weighted average map **(B, D, F, and H)** of intrusive rocks from the study area.

(Figure 5C). The Eu/Eu*values range from 0.36 to 1.30, and $(La/Yb)_N$ values are between 1.3 and 41.54, with significant REE fractionation. The chondrite-normalized REE diagram (Figure 6E) shows enrichment in LREEs, exhibiting a positive trend. The primitive-mantle-normalized trace-element spider diagram (Figure 6F) reveals enrichment in LILEs (e.g., Rb, Th, U, K, and Nd) and depletion in HFSEs (e.g., Ta, P, Eu, Ti, and Nb; Table 3).

10.3389/feart.2024.1514658

TABLE 1 Results of LA–ICP–MS zircon U–Pb analyses of intrusive rocks from the Erguna block.

Sample No.	Th ($\times10^{-6}$)	U ($\times10^{-6}$)	Th/U	$^{207}Pb/^{206}Pb$	1σ	$^{207}Pb/^{235}U$	1σ	$^{206}Pb/^{238}U$	1σ	$^{207}Pb/^{206}Pb$ Age (Ma)	1σ	$^{207}Pb/^{235}U$ Age (Ma)	1σ	$^{206}Pb/^{238}U$ Age (Ma)	1σ
FQ1															
1	222.71	567.93	0.39	0.06666	0.0016	1.32597	0.03215	0.14425	0.0019	1.32597	0.03215	0.14425	0.0019	869	11
2	276.03	509.94	0.54	0.06867	0.00224	1.31685	0.04271	0.13908	0.00203	1.31685	0.04271	0.13908	0.00203	839	11
3	203.69	493.71	0.41	0.06591	0.00132	1.31533	0.02708	0.14472	0.00184	1.31533	0.02708	0.14472	0.00184	871	10
4	452.43	635.46	0.71	0.06583	0.00123	1.31091	0.02547	0.14442	0.00181	1.31091	0.02547	0.14442	0.00181	870	10
5	195.65	431.91	0.45	0.06733	0.01317	1.33202	0.25448	0.14348	0.00752	1.33202	0.25448	0.14348	0.00752	864	42
6	335.96	520.89	0.64	0.06774	0.00184	1.32399	0.03613	0.14176	0.00194	1.32399	0.03613	0.14176	0.00194	855	11
7	313.61	643.04	0.49	0.06684	0.00146	1.32796	0.0296	0.1441	0.00186	1.32796	0.0296	0.1441	0.00186	868	10
8	452.9	645.54	0.70	0.0676	0.00142	1.31751	0.0283	0.14137	0.00181	1.31751	0.0283	0.14137	0.00181	852	10
9	161	395	0.41	0.06519	0.00724	1.31103	0.14246	0.14587	0.0045	1.31103	0.14246	0.14587	0.0045	878	25
10	213.62	434.11	0.49	0.06471	0.00159	1.31118	0.03249	0.14697	0.00194	1.31118	0.03249	0.14697	0.00194	884	11
11	495.81	470.19	1.05	0.06774	0.00109	1.33532	0.02261	0.14298	0.00175	1.33532	0.02261	0.14298	0.00175	861	10
12	142.86	302.48	0.47	0.067	0.00161	1.31786	0.03207	0.14268	0.00188	1.31786	0.03207	0.14268	0.00188	860	11
13	267.96	553.85	0.48	0.06635	0.0093	1.33034	0.18233	0.14543	0.00551	1.33034	0.18233	0.14543	0.00551	875	31
14	304.97	650.35	0.47	0.0651	0.00094	1.31743	0.02036	0.14679	0.00177	1.31743	0.02036	0.14679	0.00177	883	10
15	201.78	375.09	0.54	0.06627	0.00129	1.31442	0.02629	0.14387	0.00181	1.31442	0.02629	0.14387	0.00181	867	10
16	314.23	434.36	0.72	0.06674	0.00096	1.31333	0.02025	0.14274	0.00172	1.31333	0.02025	0.14274	0.00172	860	10
17	216.29	473.12	0.46	0.06583	0.00272	1.29768	0.05286	0.14299	0.00227	1.29768	0.05286	0.14299	0.00227	862	13
BQ1															
1	2,870.80	17,053.33	0.17	0.0564	0.0016	0.5835	0.0163	0.0750	0.0010	0.5835	0.0163	0.0750	0.0010	466	6
2	1,020.27	6,553.42	0.16	0.0563	0.0043	0.5893	0.0445	0.0760	0.0016	0.5893	0.0445	0.0760	0.0016	472	10

(Continued on the following page)

TABLE 1 *Continued* Results of LA–ICP–MS zircon U–Pb analyses of intrusive rocks from the Erguna block.

Sample No.	Th ($\times10^{-6}$)	U ($\times10^{-6}$)	Th/U	$^{207}Pb/^{206}Pb$	1σ	$^{207}Pb/^{235}U$	1σ	$^{206}Pb/^{238}U$	1σ	$^{207}Pb/^{206}Pb$ Age (Ma)	1σ	$^{207}Pb/^{235}U$ Age (Ma)	1σ	$^{206}Pb/^{238}U$ Age (Ma)	1σ
3	8,941.77	42,051.31	0.21	0.0580	0.0010	0.5886	0.0102	0.0736	0.0009	0.5886	0.0102	0.0736	0.0009	458	5
4	10,980.61	38,340.35	0.29	0.0569	0.0011	0.5870	0.0117	0.0748	0.0009	0.5870	0.0117	0.0748	0.0009	465	5
5	3,098.72	20,118.56	0.15	0.0566	0.0024	0.5908	0.0252	0.0757	0.0012	0.5908	0.0252	0.0757	0.0012	470	7
6	2,170.63	14,725.14	0.15	0.0572	0.0015	0.5879	0.0152	0.0745	0.0010	0.5879	0.0152	0.0745	0.0010	463	6
7	2,500.58	18,538.28	0.13	0.0556	0.0019	0.5871	0.0194	0.0765	0.0011	0.5871	0.0194	0.0765	0.0011	475	6
8	2,329.60	14,701.83	0.16	0.0556	0.0011	0.5808	0.0122	0.0757	0.0009	0.5808	0.0122	0.0757	0.0009	471	6
9	9,666.83	37,166.55	0.26	0.0567	0.0021	0.5899	0.0220	0.0755	0.0011	0.5899	0.0220	0.0755	0.0011	469	7
10	6,932.73	36,880.20	0.19	0.0565	0.0012	0.5940	0.0124	0.0763	0.0010	0.5940	0.0124	0.0763	0.0010	474	6
11	3,272.97	22,436.98	0.15	0.0562	0.0032	0.5948	0.0333	0.0768	0.0014	0.5948	0.0333	0.0768	0.0014	477	8
12	5,078.19	23,738.19	0.21	0.0567	0.0015	0.5891	0.0155	0.0754	0.0010	0.5891	0.0155	0.0754	0.0010	468	6
13	4,364.84	29,175.80	0.15	0.0563	0.0034	0.5881	0.0347	0.0758	0.0014	0.5881	0.0347	0.0758	0.0014	471	8
14	2,999.73	17,948.82	0.17	0.0559	0.0037	0.5889	0.0383	0.0765	0.0015	0.5889	0.0383	0.0765	0.0015	475	9
15	2,759.30	17,819.79	0.15	0.0560	0.0034	0.5945	0.0358	0.0770	0.0014	0.5945	0.0358	0.0770	0.0014	478	9
16	2,282.73	15,641.77	0.15	0.0575	0.0028	0.5942	0.0279	0.0749	0.0012	0.5942	0.0279	0.0749	0.0012	466	7
17	3,129.11	14,998.33	0.21	0.0566	0.0015	0.5972	0.0158	0.0765	0.0010	0.5972	0.0158	0.0765	0.0010	475	6
18	2,815.57	16,964.18	0.17	0.0560	0.0016	0.5968	0.0167	0.0774	0.0010	0.5968	0.0167	0.0774	0.0010	480	6
19	5,226.81	24,053.27	0.22	0.0560	0.0014	0.5903	0.0146	0.0764	0.0010	0.5903	0.0146	0.0764	0.0010	475	6
DQ1															
1	42.21	92.40	2.19	0.0528	0.0023	0.3559	0.0153	0.0489	0.0007	0.3559	0.0153	0.0489	0.0007	308	4
2	126.95	237.78	1.87	0.0520	0.0013	0.3522	0.0085	0.0491	0.0006	0.3522	0.0085	0.0491	0.0006	309	4
3	282.75	352.56	1.25	0.0531	0.0012	0.3563	0.0080	0.0486	0.0006	0.3563	0.0080	0.0486	0.0006	306	4

(Continued on the following page)

10.3389/feart.2024.1514658

TABLE 1 (*Continued*) Results of LA–ICP–MS zircon U–Pb analyses of intrusive rocks from the Erguna block.

Sample No.	Th ($\times10^{-6}$)	U ($\times10^{-6}$)	Th/U	$^{207}Pb/^{206}Pb$	1σ	$^{207}Pb/^{235}U$	1σ	$^{206}Pb/^{238}U$	1σ	$^{207}Pb/^{206}Pb$ Age (Ma)	1σ	$^{207}Pb/^{235}U$ Age (Ma)	1σ	$^{206}Pb/^{238}U$ Age (Ma)	1σ
4	158.33	313.13	1.98	0.0531	0.0023	0.3556	0.0150	0.0486	0.0007	0.3556	0.0150	0.0486	0.0007	306	4
5	141.00	245.45	1.74	0.0533	0.0016	0.3591	0.0106	0.0489	0.0006	0.3591	0.0106	0.0489	0.0006	307	4
6	228.16	396.20	1.74	0.0524	0.0012	0.3524	0.0081	0.0488	0.0006	0.3524	0.0081	0.0488	0.0006	307	4
7	141.64	395.41	2.79	0.0535	0.0019	0.3580	0.0128	0.0485	0.0007	0.3580	0.0128	0.0485	0.0007	305	4
8	572.40	521.29	0.91	0.0524	0.0010	0.3542	0.0069	0.0490	0.0006	0.3542	0.0069	0.0490	0.0006	309	4
9	143.01	231.46	1.62	0.0532	0.0016	0.3580	0.0105	0.0488	0.0006	0.3580	0.0105	0.0488	0.0006	307	4
10	80.69	134.58	1.67	0.0523	0.0021	0.3519	0.0136	0.0488	0.0007	0.3519	0.0136	0.0488	0.0007	307	4
11	208.52	283.96	1.36	0.0527	0.0013	0.3548	0.0088	0.0489	0.0006	0.3548	0.0088	0.0489	0.0006	308	4
12	253.53	262.09	1.03	0.0518	0.0019	0.3459	0.0124	0.0485	0.0007	0.3459	0.0124	0.0485	0.0007	305	4
13	237.47	299.93	1.26	0.0536	0.0027	0.3572	0.0176	0.0483	0.0008	0.3572	0.0176	0.0483	0.0008	304	5
14	383.52	330.07	0.86	0.0529	0.0013	0.3561	0.0090	0.0488	0.0006	0.3561	0.0090	0.0488	0.0006	307	4
15	163.22	169.28	1.04	0.0526	0.0018	0.3543	0.0122	0.0489	0.0007	0.3543	0.0122	0.0489	0.0007	308	4
16	72.30	133.64	1.85	0.0512	0.0015	0.3464	0.0099	0.0491	0.0006	0.3464	0.0099	0.0491	0.0006	309	4
17	168.44	263.62	1.57	0.0523	0.0012	0.3499	0.0081	0.0485	0.0006	0.3499	0.0081	0.0485	0.0006	305	4
18DN1															
1	243.44	276.13	0.88	0.0511	0.0020	0.1338	0.0065	0.0191	0.0007	255.6200	88.8750	127.4700	5.8205	122.18	4.6
2	205.55	257.12	0.8	0.0525	0.0020	0.1374	0.0046	0.0192	0.0005	309.3200	87.0275	130.6900	4.0866	122.82	3.1
3	454.51	433.17	1.05	0.0481	0.0014	0.1278	0.0040	0.0194	0.0004	105.6500	68.5125	122.1400	3.6067	123.84	2.6
4	521.29	562.92	0.93	0.0499	0.0014	0.1221	0.0044	0.0178	0.0004	190.8200	62.9525	116.9600	4.0244	113.46	2.8
5	826.39	788.38	1.05	0.0499	0.0011	0.1239	0.0030	0.0182	0.0004	187.1200	19.4400	118.6300	2.7012	116.13	2.7
6	488.37	468.09	1.04	0.0512	0.0017	0.1364	0.0058	0.0195	0.0007	255.6200	77.7650	129.8700	5.1495	124.28	4.2

(Continued on the following page)

TABLE 1 (*Continued*) Results of LA–ICP–MS zircon U–Pb analyses of intrusive rocks from the Erguna block.

Sample No.	Th (×10^{-6})	U (×10^{-6})	Th/U	^{207}Pb/^{206}Pb	1σ	^{207}Pb/^{235}U	1σ	^{206}Pb/^{238}U	1σ	^{207}Pb/^{206}Pb Age (Ma)	1σ	^{207}Pb/^{235}U Age (Ma)	1σ	^{206}Pb/^{238}U Age (Ma)	1σ
7	649.19	707.31	0.92	0.0504	0.0013	0.1237	0.0035	0.0179	0.0005	213.0400	59.2475	118.4200	3.1885	114.55	3.2
8	474.92	638.98	0.74	0.0482	0.0010	0.1215	0.0028	0.0184	0.0003	109.3500	52.7725	116.4600	2.5025	117.27	2.2
9	357.13	459.24	0.78	0.0513	0.0021	0.1244	0.0052	0.0177	0.0006	253.7700	89.8000	119.0300	4.6664	113.13	3.6
10	885.81	690.67	1.28	0.0528	0.0010	0.1287	0.0035	0.0178	0.0005	316.7300	44.4400	122.8900	3.1593	113.84	3.2

5 Discussion

5.1 Neoproterozoic–Mesozoic magmatism in the Xinlin area

Previous geochronological studies reported a wide range of ages for the intrusive rocks of the Erguna block (Table 4). At least ~929 Ma, ~887 Ma, ~850 Ma, ~819 Ma, ~792 Ma, ~764 Ma, and ~738 Ma magmatic events occurred in the Neoproterozoic Era on the Erguna block (Guo et al., 2016; Zhao et al., 2016; Yang et al., 2017). The Paleozoic magmatic activity in the Erguna block can be divided into the Early and Late Paleozoic activities. The Early Paleozoic magmatic activity can be mainly divided into four stages: ~500 Ma (Middle-Late Cambrian: 504–500 Ma), ~480 Ma (Early Ordovician: 485–475 Ma), ~460 Ma (Middle-Late Ordovician: 465–454 Ma), and ~440 Ma (Early Silurian: 439–434 Ma) (Zhao, 2017; Wu et al., 2005); the Late Paleozoic magmatic activity occurred from 330 to 241 Ma (Ju et al., 2005; Wang et al., 2012; Feng et al., 2014). The early Late Paleozoic granitic magmatism occurred between 405 and 325 Ma, which can be further refined into three stages: Early Middle Devonian (Stage I, 405 to 380 Ma), Late Devonian–Early Carboniferous (Stage II, 365 to 350 Ma), and Late Early Carboniferous (Stage III, 335 to 325 Ma) (Qian et al., 2018). The Mesozoic magmatism in the Erguna block can be divided into seven stages: ~246 Ma, ~225 Ma, ~205 Ma, ~185 Ma, ~155 Ma, ~137 Ma, and ~125 Ma (Wang et al., 2012; Tang, 2016).

To obtain a more comprehensive understanding of granitic magmatism in the northern Great Xing'an Range, we selected 66 zircon U–Pb results and combined them with the five new ages of this study. Based on this combined geochronological dataset, three stages of granitic magmatism can be identified, namely, Neoproterozoic, Paleozoic, and Mesozoic granites (Table 4). Neoproterozoic granitoids, which are rarely developed in the Erguna block, comprise hornblende gneisses and mica quartz schists, with isotopic ages ranging from 915 to 791 Ma (Table 4). Paleozoic intrusive rocks are widely distributed in the Erguna block, with ages ranging from 504 to 241 Ma. Mesozoic granitoids are widely exposed in the northern Great Xing'an Range, primarily near the Xinlin–Xiguitu suture, with ages spanning 240 to 116 Ma.

5.2 Petrogenesis

The origin and source of the magmas that formed the intrusive rocks in the Erguna block are varied and have been the focus of numerous studies (Gao et al., 2013; Hu et al., 2014; Liu et al., 2016; Wang et al., 2016; Zhao, 2017; Yang et al., 2017; Lu et al., 2020). However, debates persist regarding the petrogenesis of the Neoproterozoic–Mesozoic intrusive rocks in the Erguna block.

5.2.1 Petrogenesis of Neoproterozoic intrusive rocks

The information regarding the genesis of Neoproterozoic intrusive rocks in the Erguna block is relatively consistent, which is related to the convergence and breakup of the Rodinia supercontinent (Zhao, 2017; Lu, 2019). The approximately 887 Ma granites are similar to post-collisional granites (Liu et al., 2011;

TABLE 2 $^{40}Ar/^{39}Ar$ analytical data on muscovite samples.

Temperature step (°C)	$(^{40}Ar/^{39}Ar)_m$	$(^{36}Ar/^{39}Ar)_m$	$(^{37}Ar/^{39}Ar)_m$	^{40}Ar (%)	F ($^{40}Ar^{*}/^{39}Ar$)	^{39}Ar ($\times 10^{-14}$mol)	^{39}Ar (Cum.) (%)	Age (Ma)	±1σ (Ma)
850	33.9924	0.0147	0.016	87.14	29.6203	0.08	1.2	276.5	2.3
900	34.0037	0.0097	0.004	91.48	31.1056	0.36	5.74	289.3	1.4
950	32.3323	0.0021	0.002	98.06	31.7054	2.13	33.46	294.5	1.4
1,000	32.4243	0.0021	0.003	98.02	31.7831	1.02	16.14	295.1	1.4
1,050	32.9066	0.0018	0.003	98.32	32.3533	0.8	12.65	300	1.4
1,100	32.8158	0.0014	0.003	98.7	32.3909	0.64	10	300.3	1.4
1,150	32.4991	0.0006	0.002	99.44	32.3156	1.25	19.72	299.7	1.4
1,200	32.7877	0.002	0.031	98.17	32.1897	0.05	0.75	298.6	1.7
1,300	33.9596	0.0052	0.066	95.4	32.3997	0.02	0.35	300.4	2.5

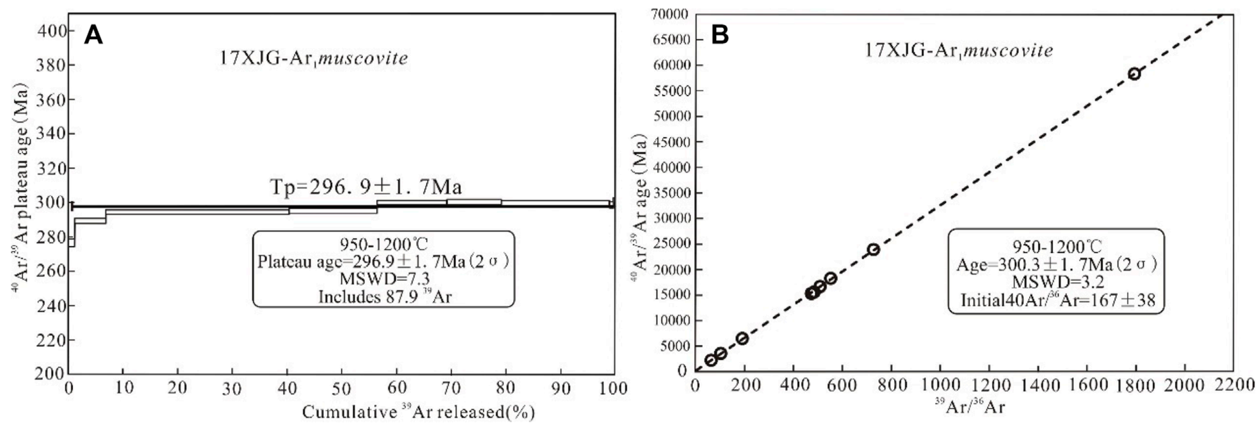

FIGURE 4
$^{40}Ar/^{39}Ar$ plateau age (Ma) **(A)** and isochron of $^{40}Ar/^{39}Ar$ age (Ma) **(B)** of muscovite from the study area.

Zhao et al., 2016), whereas the 850–737 Ma granitoids are generally similar to A-type granites, and the magmas could have originated not only from the partial melting of a depleted lower crust that accreted during the Meso-Neoproterozoic, with a contribution of ancient crustal materials in their petrogenesis, but also from the partial melting of the residual ancient mafic crustal material (Tang et al., 2013; Zhao et al., 2016).

The Neoproterozoic Xinghuadukou rock group hornblende gneisses in the study area exhibit high $Mg^{\#}$ values (average 50.25), which rules out the possibility that they were derived from partial melting of the lower crust. The hornblende gneisses show Nb contents ranging from 8.20 to 21.70 ppm, higher than those of N-MORB (typically 2–3 ppm; Sun and McDonough, 1989). The TiO_2 contents of hornblende gneisses range from 0.57% to 0.62%, lower than those of OIB (≈2.68%; Ewart et al., 1998). The hornblende gneisses are also characterized by relatively high V, Sr, Ni, Co, and Cr contents and low Si content, suggesting a mantle-derived origin.

5.2.2 Petrogenesis of Early Paleozoic intrusive rocks

The Early Paleozoic intermediate–acidic rocks in the Erguna block mainly originated from the partial melting of the newly accreted lower crust, with the participation of some residual ancient crustal materials; the primitive magma of the basic rocks mainly originated from the partial melting of the depleted lithospheric mantle that was metasomatized by subducting fluids (Zhao, 2017). The collision granite magma on the northern edge of the Erguna block originated from the mantle during the Early Paleozoic and was involved in the crustal material (Wu et al., 2005; Lu et al., 2022).

The Early Paleozoic intrusive rocks in the Xinlin area are predominantly the Early Ordovician gabbros, exhibiting high $Mg^{\#}$ values (average 59.75), which rules out the partial melting of the lower crust as their source. The gabbros have Nb contents of 1.40 to 6.90 ppm (average 4.64 ppm), which is higher than those of N-MORB (generally 2–3 ppm; Sun and McDonough, 1989).

10.3389/feart.2024.1514658

TABLE 3 Geochemical data on intrusive rocks from the study area.

Sample No.	FQ1	FQ2	FQ4	FQ5	FQ7	FQ8	BQ1	BQ2	BQ3	BQ4	BQ5	DQ1	DQ2	DQ3
Rock type	Hornblende gneiss						Gabbro					Monzonitic granite		
Stratigraphic code	Pt_3						O_1					C_2		
SiO_2	62.73	62.24	62.72	62.19	61.90	63.76	36.01	34.49	38.24	34.23	43.68	76.06	76.14	75.26
TiO_2	0.57	0.60	0.60	0.58	0.62	0.61	5.65	6.77	4.43	5.02	1.33	0.05	0.06	0.02
Al_2O_3	16.48	16.20	16.82	16.96	17.04	16.46	12.16	10.36	14.41	14.00	21.22	13.22	12.88	13.18
TFe_2O_3	11.22	10.9	10.65	9.53	11.58	10.42	20.64	23.61	19.15	18.70	10.21	1.84	1.86	1.94
MnO	0.07	0.06	0.05	0.06	0.08	0.06	0.24	0.25	0.23	0.20	0.14	0.02	0.02	0.02
MgO	3.74	4.06	3.28	3.55	3.47	3.67	8.32	7.81	8.00	4.18	6.15	0.09	0.10	0.04
CaO	0.94	1.04	0.74	1.16	0.95	0.73	10.85	11.80	9.72	14.25	12.00	0.29	0.37	0.24
Na_2O	3.00	3.59	2.70	4.34	2.65	1.96	0.90	0.79	1.40	1.34	1.96	2.94	2.92	2.92
K_2O	4.13	3.83	4.49	3.04	4.04	4.53	0.23	0.11	0.24	0.37	0.46	5.77	5.39	6.31
P_2O_5	0.24	0.24	0.24	0.23	0.25	0.25	0.03	0.04	0.03	1.55	0.03	0.04	0.04	0.03
LOI	2.83	2.37	2.64	2.95	2.72	2.66	5.17	3.42	4.06	5.75	3.11	0.53	0.66	0.34
Total	113.93	113.27	112.55	110.79	113.74	112.45	159.40	169.65	155.59	152.20	129.11	102.12	101.61	101.86
σ	2.58	2.86	2.62	2.84	2.37	2.03	0.18	0.10	0.57	0.33	8.61	2.29	2.08	2.64
A/NK	1.48	1.36	1.58	1.35	1.63	1.74	7.03	7.30	5.62	5.37	5.70	1.19	1.21	1.13
A/CNK	1.75	1.61	1.81	1.63	1.95	2.03	0.57	0.45	0.71	0.49	0.83	1.14	1.14	1.09
Mg#	43.72	46.46	41.79	46.47	59.61	63.44	30.78	26.73	31.54	19.78	39.92	10.24	11.14	4.58
Cs	4.08	3.01	3.40	2.00	4.98	5.11	0.80	0.37	0.66	1.60	0.87	2.86	3.03	4.12
Rb	161.00	131.00	183.00	111.00	173.00	177.00	6.90	2.00	7.60	11.30	16.90	160.50	152.00	170.50
Sr	108.50	139.00	118.50	130.00	202.00	143.50	396.00	334.00	449.00	794.00	835.00	77.80	85.50	77.20
Ba	1,285.00	1,115.00	1,140.00	644.00	1,195.00	794.00	56.10	44.40	87.70	105.50	185.00	373.00	397.00	349.00
Ga	19.60	19.90	20.70	21.70	21.30	19.80	18.90	20.40	18.40	23.20	18.40	14.40	15.00	15.90

(Continued on the following page)

TABLE 3 (*Continued*) Geochemical data on intrusive rocks from the study area.

Sample No.	FQ1	FQ2	FQ4	FQ5	FQ7	FQ8	BQ1	BQ2	BQ3	BQ4	BQ5	DQ1	DQ2	DQ3
Rock type	Hornblende gneiss						Gabbro					Monzonitic granite		
Stratigraphic code	Pt_3						O_1					C_2		
Nb	9.30	11.20	10.90	8.20	21.70	8.70	5.00	6.90	4.20	5.70	1.40	8.10	10.10	4.40
Ta	0.40	0.50	0.60	0.40	1.00	0.40	0.40	0.50	0.30	0.40	0.10	0.80	1.10	0.50
Zr	226.00	204.00	215.00	197.00	224.00	262.00	46.00	51.00	37.00	50.00	27.00	70.00	76.00	65.00
Hf	6.10	5.40	5.90	5.30	5.90	6.90	1.60	1.70	1.10	1.50	0.70	2.30	2.80	2.40
Th	9.31	17.25	10.15	5.40	12.85	5.29	0.23	0.15	0.19	0.75	0.52	7.97	10.75	9.07
V	103.00	105.00	115.00	119.00	110.00	99.00	989.00	891.00	777.00	623.00	242.00	5.00	6.00	11.00
Cr	30.00	30.00	30.00	30.00	30.00	30.00	80.00	70.00	130.00	20.00	60.00	10.00	20.00	10.00
Co	11.80	9.70	11.40	11.20	10.90	10.80	69.40	77.20	72.10	45.80	39.20	0.60	0.50	0.40
Ni	13.80	14.00	15.10	13.10	14.00	14.50	86.30	82.30	101.00	26.00	30.60	0.90	0.90	1.00
Li	17.30	24.40	19.70	24.10	29.30	29.40	16.30	13.20	19.80	10.60	15.90	5.30	5.70	5.30
Sc	12.00	11.60	13.40	9.40	13.40	13.00	48.50	54.80	31.70	38.30	14.20	1.80	2.40	1.20
U	1.00	0.80	1.60	1.40	3.00	1.30	0.10	0.10	0.10	0.30	0.10	1.20	1.40	1.30
K	34,285.15	31,794.71	37,273.69	25,236.53	33,538.02	37,605.75	1,909.34	913.16	1,992.36	3,071.55	3,818.69	47,899.60	44,745.03	52,382.40
Ti	3,416.57	3,596.39	3,596.39	3,476.51	3,716.27	3,656.33	33,866.04	40,579.31	26,553.38	30,089.83	7,972.01	299.70	359.64	119.88
P	1,047.32	1,047.32	1,047.32	1,003.68	1,090.96	1,090.96	130.91	174.55	130.91	6,763.92	130.91	174.55	174.55	130.91
La	48.10	64.50	50.00	19.90	44.80	18.40	2.80	2.70	2.60	16.60	3.60	12.50	15.90	13.00
Ce	97.80	118.00	102.00	43.80	91.00	43.30	7.70	8.40	6.30	45.30	7.36	24.60	33.40	26.80
Pr	12.25	11.65	12.50	5.04	10.65	7.12	1.21	1.49	0.95	6.80	1.10	2.64	3.81	3.28
Nd	45.90	41.20	45.40	20.00	39.40	30.80	6.80	8.95	5.00	35.15	5.30	10.10	14.10	12.40
Sm	7.45	5.51	7.21	3.46	6.80	5.98	2.18	3.07	1.56	9.15	1.31	2.01	2.80	2.61
Eu	1.57	1.30	1.56	0.77	1.23	1.22	0.99	1.17	0.95	2.69	0.94	0.37	0.48	0.45

(Continued on the following page)

TABLE 3 (*Continued*) Geochemical data on intrusive rocks from the study area.

Sample No.	FQ1	FQ2	FQ4	FQ5	FQ7	FQ8	BQ1	BQ2	BQ3	BQ4	BQ5	DQ1	DQ2	DQ3
Rock type	Hornblende gneiss						Gabbro					Monzonitic granite		
Stratigraphic code	Pt_3						O_1					C_2		
Gd	5.38	3.87	5.75	2.87	5.03	4.99	2.93	3.80	1.82	10.10	1.33	1.74	2.16	2.07
Tb	0.76	0.53	0.80	0.41	0.75	0.73	0.45	0.59	0.29	1.42	0.20	0.25	0.31	0.30
Dy	4.42	2.87	4.50	2.47	4.46	4.23	2.85	3.62	1.97	8.00	1.26	1.43	1.54	1.72
Ho	0.90	0.54	0.90	0.47	0.91	0.89	0.58	0.77	0.37	1.57	0.24	0.29	0.31	0.33
Er	2.53	1.56	2.50	1.32	2.57	2.46	1.59	2.09	1.02	4.06	0.70	0.82	0.84	0.95
Tm	0.37	0.22	0.38	0.19	0.40	0.37	0.22	0.28	0.14	0.50	0.10	0.14	0.13	0.14
Yb	2.43	1.42	2.40	1.31	2.37	2.34	1.35	1.65	0.98	2.84	0.62	0.94	0.89	0.97
Lu	0.39	0.23	0.37	0.21	0.36	0.36	0.19	0.24	0.15	0.39	0.10	0.14	0.14	0.15
Y	24.40	15.30	26.30	13.00	25.00	23.90	14.40	18.90	9.60	41.00	6.60	9.00	9.40	10.10
ΣREE	254.65	268.70	262.57	115.22	235.73	147.09	46.24	57.72	33.70	185.57	30.76	66.97	86.21	75.27
LR/HR	5.12	9.12	4.98	4.18	4.63	2.65	0.88	0.81	1.06	1.66	1.76	3.54	4.48	3.50
δEu	0.72	0.82	0.72	0.73	0.62	0.66	1.20	1.05	1.72	0.85	2.16	0.41	0.40	0.36
$(La/Yb)_N$	13.35	30.62	14.05	10.24	12.74	5.30	1.40	1.10	1.79	3.94	3.91	8.97	12.04	9.04

Sample No.	WQ15	WQ16	WQ17	P_{52}GS3	P_{60}GS3	GS1179	GS4071	GS2065	GS4075	P_{54}GS1	P_{50}GS9	P_{52}GS30	P_{63}GS6
Rock type	Potash feldspar granite			Syenogranite	Monzonitic granite		Syenogranite		Monzonitic granite		Alkali feldspar granite	Monzoniti granite	Diorite
Stratigraphic code	C_2			P_1			T_3J_1				K_1		
SiO_2	74.37	73.67	73.96	75.78	69.83	70.13	75.69	73.70	71.66	70.66	77.47	76.11	57.87
TiO_2	0.17	0.17	0.17	0.07	0.22	0.37	0.16	0.14	0.13	0.31	0.06	0.10	1.03

(Continued on the following page)

TABLE 3 (*Continued*) Geochemical data on intrusive rocks from the study area.

Sample No.	WQ15	WQ16	WQ17	P_{52}GS3	P_{60}GS3	GS1179	GS4071	GS2065	GS4075	P_{54}GS1	P_{50}GS9	P_{52}GS30	P_{63}GS6
Rock type	Potash feldspar granite			Syenogranite	Monzonitic granite		Syenogranite		Monzonitic granite		Alkali feldspar granite	Monzonitic granite	Diorite
Stratigraphic code	C_2			P_1			T_3J_1				K_1		
Al_2O_3	13.69	13.38	13.68	12.38	16.26	15.89	12.91	13.13	14.50	14.66	11.68	12.13	16.72
TFe_2O_3	3.04	3.42	3.34	1.51	1.71	1.34	1.51	2.38	1.85	2.48	1.40	1.34	6.84
MnO	0.05	0.07	0.05	0.08	0.08	0.07	0.08	0.08	0.05	0.08	0.05	0.07	0.11
MgO	0.27	0.28	0.30	0.21	0.40	0.99	0.22	0.26	0.16	0.34	0.15	0.20	3.50
CaO	0.77	1.14	0.73	0.67	0.70	4.18	0.34	0.73	0.42	1.10	0.26	0.69	4.17
Na_2O	3.66	3.68	3.74	4.00	5.06	4.73	3.40	4.30	3.98	3.93	3.88	3.22	4.13
K_2O	4.44	4.42	4.54	4.48	4.63	1.30	4.93	4.66	5.78	5.28	4.51	5.37	3.50
P_2O_5	0.06	0.06	0.06	0.02	0.07	0.11	0.02	0.03	0.02	0.12	0.01	0.03	0.35
LOI	0.65	1.15	0.63	0.59	0.79	0.54	0.90	0.66	0.92	0.96	0.58	0.60	1.73
Total	103.50	103.62	103.82	99.69	99.66	99.57	100.11	99.98	99.38	99.85	99.98	99.79	99.66
σ	2.09	2.14	2.21	2.19	3.50	1.34	2.12	2.62	3.32	3.07	2.04	2.23	3.92
A/NK	1.26	1.23	1.24	1.08	1.22	1.73	1.18	1.08	1.13	1.20	1.04	1.09	1.58
A/CNK	1.12	1.04	1.10	0.98	1.11	0.95	1.12	0.98	1.07	1.03	1.00	0.98	0.92
Mg#	17.14	16.01	17.32	24.46	35.22	63.24	25.31	20.26	16.80	24.18	19.93	25.74	54.38
Cs	5.82	4.26	7.31	2.02	2.91	0.64	2.15	1.12	3.36	2.27	3.18	4.05	2.28
Rb	206.00	204.00	218.00	136.00	102.00	40.50	167.00	136.00	108.00	143.00	227.00	182.00	118.00
Sr	119.00	127.50	113.00	61.50	542.00	581.00	40.60	81.50	68.00	182.00	13.40	63.30	968.00
Ba	442.00	439.00	450.00	341.00	1,123.00	616.00	261.00	256.00	649.00	653.00	30.20	246.00	826.00
Ga	17.80	17.60	17.70	14.50	20.10	12.70	17.00	20.60	20.30	18.50	25.00	14.60	22.00

(Continued on the following page)

10.3389/feart.2024.1514658

TABLE 3 (*Continued*) Geochemical data on intrusive rocks from the study area.

Sample No.	WQ15	WQ16	WQ17	P_{52}GS3	P_{60}GS3	GS1179	GS4071	GS2065	GS4075	P_{54}GS1	P_{50}GS9	P_{52}GS30	P_{63}GS6
Rock type	Potash feldspar granite			Syenogranite	Monzonitic granite		Syenogranite		Monzonitic granite		Alkali feldspar granite	Monzonitic granite	Diorite
Stratigraphic code	C_2			P_1			T_3J_1				K_1		
Nb	21.60	22.80	22.20	9.35	6.41	8.20	19.20	19.40	8.15	22.80	31.50	13.40	10.40
Ta	2.70	3.00	3.00	0.95	0.47	0.62	1.67	1.29	0.65	1.82	2.39	1.58	0.72
Zr	120.00	124.00	113.00	106.00	148.00	121.00	192.00	272.00	317.00	280.00	145.00	99.80	352.00
Hf	3.70	3.90	3.50	3.61	3.81	3.44	5.29	7.37	7.36	6.29	6.64	3.63	8.46
Th	16.80	17.75	16.55	14.60	7.24	10.40	17.70	17.60	12.60	13.70	22.60	24.40	21.00
V	12.00	11.00	12.00	2.73	11.70	32.00	3.01	6.29	1.91	12.40	<1	6.71	126.00
Cr	20.00	10.00	20.00	8.31	5.37	8.71	6.42	8.61	4.11	8.01	6.23	6.65	45.50
Co	1.30	1.50	1.50	1.11	1.70	2.77	1.16	1.90	0.71	2.24	0.77	1.60	19.00
Ni	0.90	0.90	0.90	3.68	2.47	4.33	2.00	3.55	1.50	2.96	2.09	3.27	34.80
Li	26.40	31.20	33.80	6.69	16.90	13.60	11.90	3.49	13.20	13.40	3.31	26.00	7.36
Sc	3.50	3.30	3.20	1.74	1.61	3.52	3.09	4.60	3.46	3.99	0.62	1.73	10.50
U	4.80	6.00	6.00	0.73	1.21	2.07	2.28	2.33	2.33	3.67	5.38	5.57	3.75
K	36,858.62	36,692.59	37,688.76	37,190.68	38,435.90	10,791.94	40,926.35	38,684.94	47,982.61	43,831.87	37,439.72	44,579.00	29,055.22
Ti	1,018.98	1,018.98	1,018.98	419.58	1,318.68	2,217.78	959.04	839.16	779.22	1,858.14	359.64	599.40	6,173.81
P	261.83	261.83	261.83	87.28	305.47	480.02	87.28	130.91	87.28	523.66	43.64	130.91	1527.34
La	28.20	25.60	28.60	27.40	22.80	22.90	35.70	23.00	39.30	48.20	11.40	19.40	40.60
Ce	54.60	50.40	54.90	46.10	46.60	38.90	72.80	63.10	105.00	91.80	25.70	37.20	85.70
Pr	5.17	5.31	5.03	5.31	4.15	4.42	8.74	4.88	7.68	10.40	4.45	4.39	10.70
Nd	17.90	18.60	18.00	18.00	13.80	15.20	31.40	16.90	26.00	36.70	19.00	15.30	41.00

(Continued on the following page)

10.3389/feart.2024.1514658

TABLE 3 (*Continued*) Geochemical data on intrusive rocks from the study area.

Sample No.	WQ15	WQ16	WQ17	P_{52}GS3	P_{60}GS3	GS1179	GS4071	GS2065	GS4075	P_{54}GS1	P_{50}GS9	P_{52}GS30	P_{63}GS6
Rock type	Potash feldspar granite			Syenogranite	Monzonitic granite		Syenogranite		Monzonitic granite		Alkali feldspar granite	Monzonitic granite	Diorite
Stratigraphic code	C_2			P_1			T_3J_1				K_1		
Sm	3.28	3.39	3.31	2.76	1.84	2.40	5.86	2.85	3.53	6.25	6.02	2.89	6.63
Eu	0.44	0.42	0.40	0.49	0.73	0.90	0.41	0.36	0.84	1.15	0.19	0.46	1.52
Gd	3.09	3.06	2.81	2.52	1.54	2.20	5.46	3.01	3.30	5.75	6.94	2.69	5.58
Tb	0.49	0.54	0.47	0.34	0.18	0.27	0.81	0.50	0.47	0.85	1.31	0.42	0.68
Dy	2.81	3.48	2.88	1.82	0.72	1.32	4.66	3.24	2.37	4.68	8.80	2.37	3.00
Ho	0.56	0.74	0.54	0.36	0.13	0.25	0.92	0.71	0.49	0.94	1.82	0.50	0.54
Er	1.62	2.29	1.56	1.19	0.42	0.75	2.85	2.31	1.61	2.95	5.50	1.57	1.59
Tm	0.25	0.35	0.24	0.19	0.06	0.10	0.42	0.38	0.25	0.44	0.85	0.26	0.21
Yb	1.78	2.48	1.64	1.29	0.37	0.73	2.81	2.64	1.72	2.92	5.69	1.82	1.33
Lu	0.26	0.35	0.24	0.19	0.06	0.12	0.43	0.40	0.27	0.45	0.83	0.28	0.19
Y	18.50	24.60	18.50	11.00	4.18	7.79	28.10	23.40	14.20	30.60	54.60	16.50	16.20
ΣREE	138.95	141.61	139.12	107.96	97.58	98.25	201.37	147.68	207.03	244.08	153.10	106.05	215.47
LR/HR	3.73	2.74	3.82	12.67	25.84	14.76	8.44	8.42	17.40	10.25	2.10	8.04	14.19
δEu	0.42	0.39	0.39	0.56	1.30	1.19	0.22	0.38	0.75	0.58	0.09	0.50	0.75
$(La/Yb)_N$	10.68	6.96	11.76	14.32	41.54	21.15	8.57	5.87	15.40	11.13	1.35	7.19	20.58

Note: $Mg^{\#} = 100\{[\omega(MgO)/40]/[\omega(MgO)/40 + 0.8998\omega(TFe_2O_3)/72]\}$; $\delta = [\omega(Na_2O) + \omega(K_2O)]^2/[\omega(SiO_2) - 43]$. The unit of the mass fraction of major elements is wt.%. The unit of the mass fraction of trace elements is ppm.

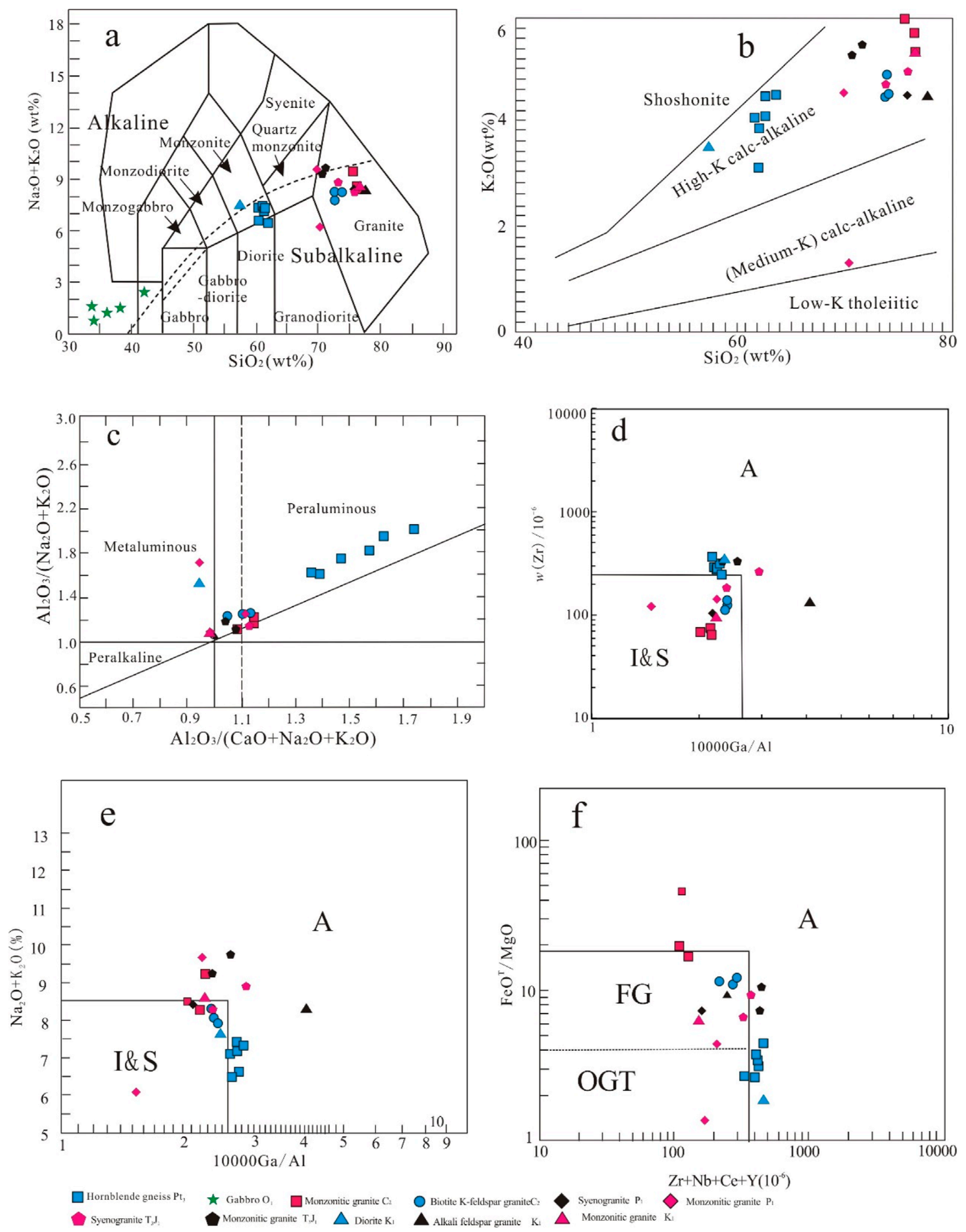

FIGURE 5
(A) TAS diagram, **(B)** K_2O *versus* SiO_2 diagram, **(C)** A/CNK *versus* A/NK diagram, and **(D–F)** discrimination diagrams for A-type granite for intrusive rocks of the study area are from Irvine and Baragar (1971), Peccerillo and Taylor (1976), Maniar and Piccoli (1989), Whalen et al. (1987), and Frost et al. (2001), respectively.

The TiO_2 contents of the gabbros are between 1.33% and 6.77% (average 4.64%), which is higher than those of OIB (≈2.68%; Ewart et al., 1998). Additionally, these gabbros yielded an average Rb/Sr value of 0.015, which is close to the primitive mantle value (0.03; Sun and McDonough, 1989). They also exhibit low Si and high Sr (334–835 ppm), Ni (26–101 ppm), Co (39.2–77.2 ppm), and Cr (20–130 ppm) contents, further supporting their origin from the mantle.

5.2.3 Petrogenesis of the intermediate–acidic intrusive rocks

In the Triassic to Early Jurassic period, the primitive magma of basic intrusive rocks originated from the partial melting of the depleted lithospheric mantle, and intermediate–acidic intrusive rocks originated from the partial melting of the newly accreted lower crust and were mixed with a small amount of ancient continental crust material (Tang et al., 2014; Tang, 2016). The Early Jurassic

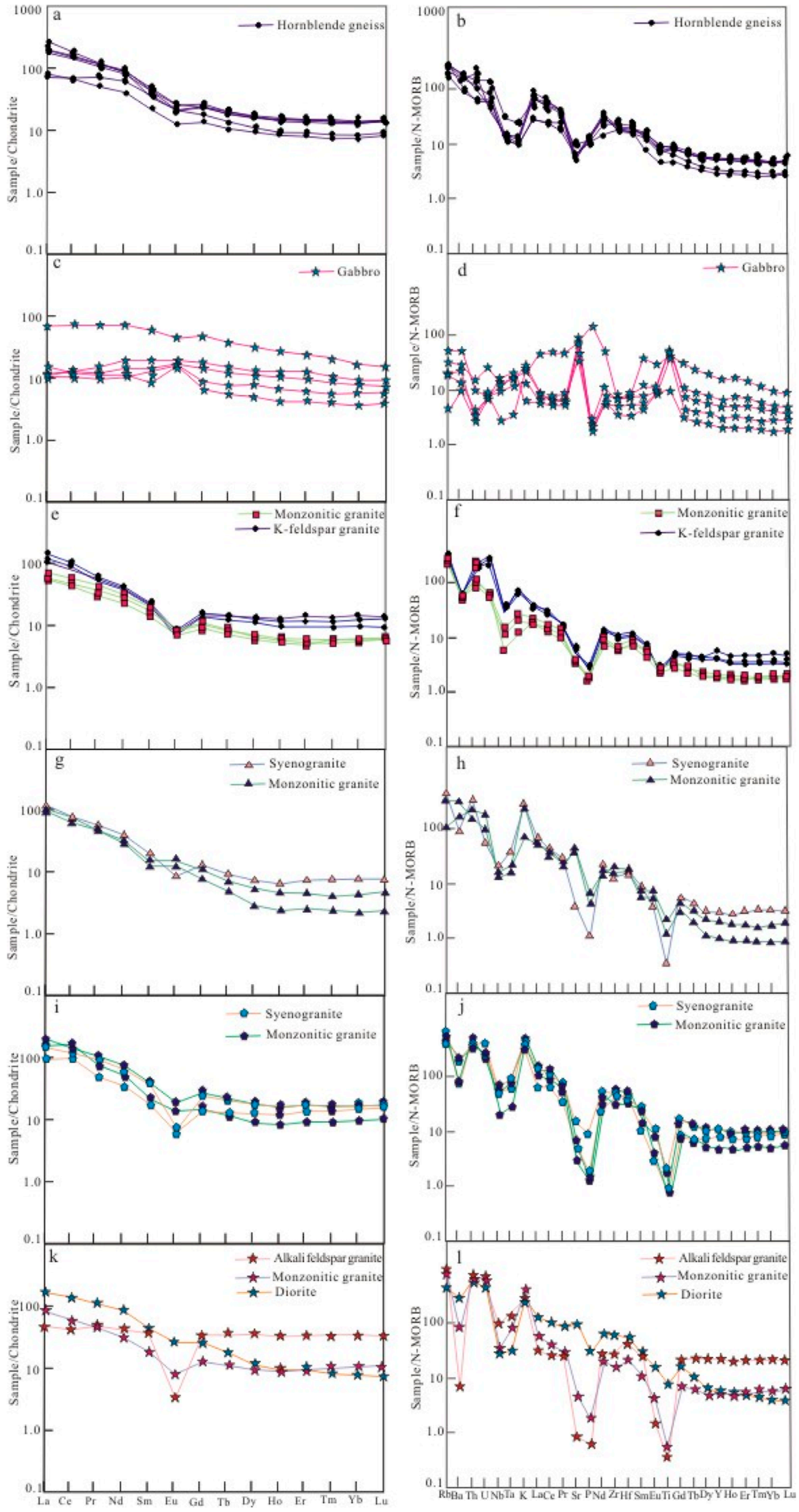

FIGURE 6
REE patterns **(A,C,E,G,I, and K)** and primary mantle trace-element patterns **(B,D,F,H,J, and L)** for intrusive rocks in the study area. Chondrite and N-MORB normalizing values are from Boynton (1984) and Sun and McDonough (1989), respectively.

granitic magmas formed from the partial melting of the felsic crust (Wang et al., 2016; Tang, 2016) or crust–mantle mixing (Dai et al., 2013); the Late Jurassic granitic magmas formed as a result of the dismantling/melting of the thickened lower crust in a collisional orogenic belt (Wu et al., 2008) or from crust–mantle interaction (Dai et al., 2013; Hu et al., 2014; Tang, 2016); and

TABLE 4 Geochronological data on the intrusive rocks in the Erguna block.

Order	Era	Sample	GPS location	Pluton	Lithology	Age (Ma)	Reference
1	Neoproterozoic	FQ1	125°13′30″, 51°48′35″	Study area	Hornblende gneiss	864.9 ± 5.4	
2		HP28		Mohe	Two mica quartz schist	892 ± 20	Wu. (2006)
3		12ER28-1		Mangui	Biotite monzogranite	850 ± 9	Zhao et al. (2016)
4		13ER12-1		Mangui	Monzogranite	846 ± 5	Zhao et al. (2016)
5		13ER13-1		Mangui	Alkali feldspar granite	846 ± 5	Zhao et al. (2016)
6		14ER17-1		Mohe	Biotite monzogranite	791 ± 5	Zhao et al. (2016)
7		14ER11-1		Bishui	Alkali feldspar granite	795 ± 4	Zhao et al. (2016)
8		14ER13-1		Amuer	Granodiorite	793 ± 4	Zhao et al. (2016)
9		FHS-01		Xinlin	Tonalite	807.7 ± 2. 2	Guo et al. (2016)
10		SPM4TC07	124°56.083′, 51°50.034′	Bowuleshan	Gneissic granite	915 ± 3	Yang et al. (2017)
11		HQG	124°51.364′, 51°52.936′	Hongqigou	Amphibolite	904 ± 4	Yang et al. (2017)
12	Paleozoic	BQ1		Study area	gabbro	470.0 ± 2.9	
13		DQ1		Study area	monzonitic granite	306.9 ± 1.9	
14		17XJG-Ar_1		Study area	muscovite	296.9 ± 1.7	
15		HP22B		Mohe	granodiorite	450 ± 15	Wu. (2006)
16		GW03090	124°24′06″, 52°18′09″	Tahe	Alkali feldspar granite	493 ± 5	Ge et al. (2005)
17		GW03070	124°42′16, ″52°21′16″	Tahe	Syenogranite	494 ± 9	Ge et al. (2005)
18		GW03036	124°47′48″, 52°21′42″	Tahe	Syenogranite	480 ± 4	Ge et al. (2005)
19		GW03035	124°47′48″, 52°21′42″	Tahe	Hornblende gabbro	490 ± 3	Ge et al. (2005)
20		GW03085	124°32′43″, 52°18′35″	Tahe	Biotite monzogranite	485 ± 3	Ge et al. (2005)
21		ML-7		Luoguhe	Quartz diorite	517 ± 9	Wu et al. (2005)
22		ML-14	121°42′11″, 48°48′26″	Luoguhe	Monzogranite	504 ± 8	Wu et al. (2005)
23	Mesozoic	18DN1		Study area	Diorite	117.8 ± 3.1	
24		13ER13-6	122°05′33″, 52°03′26″		Gabbro-diorite	227 ± 6	Tang. (2016)
25		11ER17-1	120°02′19″, 51°03′14″		Syenogranite	242 ± 3	Tang. (2016)
26		11ER9-1	119°34′09″, 50°42′25″		Syenogranite	224 ± 2	Tang. (2016)
27		12ER19-1	120°48′47″, 51°29′21″		Syenogranite	205 ± 1	Tang. (2016)
28		11ER21-1	119°49′04″, 51°13′14″		Monzonite	155 ± 1	Tang. (2016)
29		11ER16-6	119°41′05″, 50°58′38″		Monzonitic granite	125 ± 2	Tang. (2016)
30		GW03181	123°08′56″, 52°38′58″	Lvlin	Quartz diorite	192 ± 3	Wu et al. (2011)
31		GW03193	123°05′00″, 52°27′59″	Lvlin	Alkali feldspar granite	187 ± 2	Wu et al. (2011)
32		GW03251	121°53′21″, 52°38′14″	Fukeshan	Monzogranite	189 ± 2	Wu et al. (2011)
33		GW03269	122°03′54″, 52°07′36″	Mangui	Syenogranite	189 ± 2	Wu et al. (2011)

(Continued on the following page)

TABLE 4 (*Continued*) Geochronological data on the intrusive rocks in the Erguna block.

Order	Era	Sample	GPS location	Pluton	Lithology	Age (Ma)	Reference
34		GW03290	121°53′39″, 52°05′41″	Mangui	Monzogranite	187 ± 3	Wu et al. (2011)
35		GW04114	120°39′56″, 51°19′54″	Moerdaoga	Monzogranite	198 ± 2	Wu et al. (2011)
36		GW04126	120°22′03″, 51°19′08″	Bajianfang	Monzogranite	196 ± 3	Wu et al. (2011)
37		GW05067	126°08′25″, 52°31′50″	Zhengqi	Granodiorite	190 ± 1	Sui et al. (2007)
38		GW05099	125°38′40″, 52°02′43″	Hanjiayuanzi	Diorite	188 ± 2	Sui et al. (2007)
39		FW04-414	123°27′33″, 48°15′41″	Dechang	Monzogranite	166 ± 2	Wu et al. (2011)
40		FW04-416 cr54j	123°26′00″, 48°40′23″	Sanchahe	Monzogranite	179 ± 1	Wu et al. (2011)
41		FW04-417	123°13′27″, 48°37′57″	Sanchahe	Monzogranite	157 ± 2	Wu et al. (2011)
42		GW04015	122°05′42″, 48°36′48″	Yalu	Monzogranite	145 ± 5	Wu et al. (2011)
43		GW04465	124°22′30″, 50°22′59″	Jiageda	Granodiorite	165 ± 1	Wu et al. (2011)
44		GW04512	125°39′09″, 50°23′02″	Sankuanggou	Granodiorite	177 ± 3	Ge et al. (2015)
45		GW04516	125°43′50″, 50°22′50″	Huaduoshan	Granodiorite	176 ± 3	Ge et al. (2015)
46		GW05085	126°12′46″, 52°00′23″	Xinghua	Granodiorite	178 ± 1	Sui et al. (2007)
47		GW05067	126°08′25″, 52°31′50″	Zhengqi	Granodiorite	190 ± 1	Sui et al. (2007)
48		GW05129	127°05′00″, 50°53′41″	Baishilazi	Granodiorite	170 ± 2	Sui et al. (2007)
49		GW07012	126°31′04″, 48°50′48″	Molabushan	Monzogranite	169 ± 3	Zhang et al. (2008)
50		GW07017	126°22′23″, 49°01′58″	Chaoyanglinchang	Monzogranite	187 ± 6	. Zhang et al. (2008)
51		GW07019	126°21′44″, 48°56′22″	Chaoyanglinchang	Monzogranite	171 ± 4	Zhang et al. (2008)
52		2002XKL-2	126°54′29″, 50°13 29″	Heihe	Granodiorite	164 ± 4	Miao et al. (2004)
53		2002XKL-7	126°47′45″, 50°15′25″	Heihe	Granodiorite	167 ± 4	Miao et al. (2004)
54		Gs1663		Tahe	Granodiorite	131 ±1	Niu et al. (2016)
55		Gs27		Tahe	Quartz diorite	130 ± 1	Niu et al. (2016)
56		0075-7	124°19′26″, 51°36′23″	Xinlinzhen	Granodiorite	132 ± 3	Zhang et al. (2008)
57		FW04-403	123°45′44″, 49°33′41″	Longtou	Monzogranite	129 ± 2	Wu et al. (2011)
58		FW04-413	123°45′33″, 49°10′38″	Nuomin	Monzogranite	130 ± 1	Wu et al. (2011)
59		Z10-02	122°12′43″, 47°10′35″	Haduohe	Syenite granite	127 ± 1	Gao et al. (2013)
60		Z10-03	122°10′54″, 47°10′28″	Haduohe	Granodiorite	126 ± 1	Gao et al. (2013)
61		Z10-04	122°10′54″, 47°10′28″	Haduohe	Quartz diorite	131 ± 1	Gao et al. (2013)
62		Z10-05	122°03′00″, 47°05′40″	Haduohe	Monzonitic granite	130 ± 1	Gao et al. (2013)
63		0116-1	122°14′40″, 51°26′18″	Niuerhe	Alkali feldspar granite	125 ± 2	Wu et al. (2011)
64		GW03285	122°05′33″, 52°03′27″	Mangui	Dolerite	132 ± 2	Wu et al. (2011)
65		FW04-405	123°21′29″, 49°33′03″	Dalaibin	Monzogranite	139 ± 1	Wu et al. (2011)
66		FW04-407	123°46′04″, 49°14′31″	Yilinongchang	Monzogranite	131 ± 1	Wu et al. (2011)

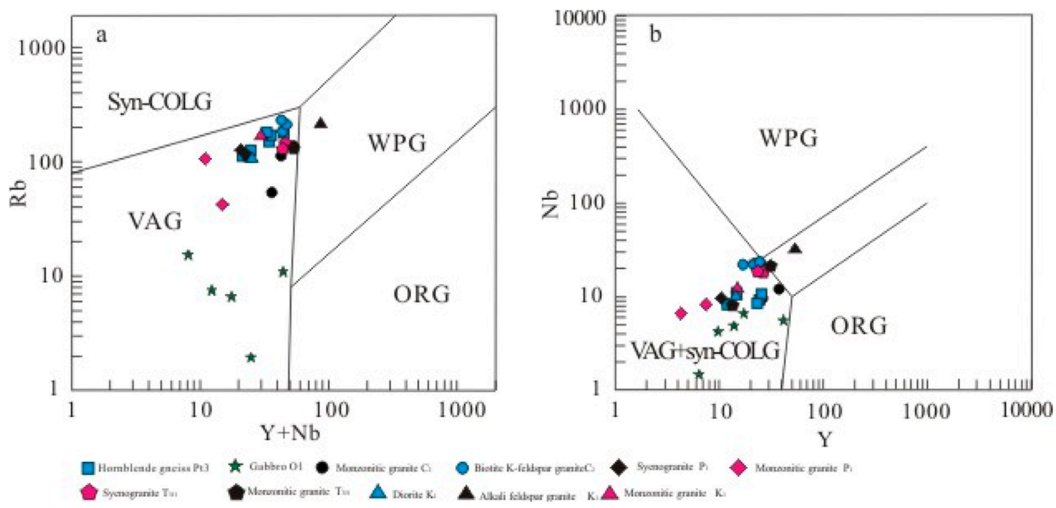

FIGURE 7
(A) (Y + Nb) vs. Rb diagram and **(B)** Nb vs. Y diagram for intrusive rocks in the study area are from Pearce et al. (1984).

the Early Cretaceous granitic magmas were derived from the partial melting of crustal material (Wu et al., 2008; Gao et al., 2013; Shi et al., 2013; Niu et al., 2016), where the lithospheric mantle was metasomatized by subduction-related fluids, forming the parent magmas to the diorites. This process may have involved the partial melting of the subducted plate and metasomatism of the lithospheric mantle by sediment-derived fluids (Liu et al., 2016; Chai et al., 2018).

The Late Carboniferous, Early Permian, Late Triassic–Early Jurassic, and Early Cretaceous intrusive rocks in the study area are predominantly intermediate–acidic, peraluminous, and a part of the high-K calc-alkaline series; the major elements show high SiO_2 content and low Fe_2O_{3T} and $Mg^{\#}$ values (average 24.12), and the trace elements are enriched in LREEs, such as Rb, Th, U, K, Nd, Zr, and Hf, and relatively depleted in HREEs, such as Ba, Nb, Sr, P, Eu, and Ti. The negative Eu anomalies of the intermediate–acidic intrusive rocks indicate that the plagioclases likely originate from the residual phases (Lightfoot et al., 1987). The intermediate–acidic intrusive rocks yield an average Rb/Sr value of 2.62, which is close to the crustal ratio (0.15) but higher than that of the primitive mantle (0.03), E-MORB (0.033), and OIB (0.047) (Sun and McDonough, 1989), and these geochemical features suggest that they were derived from the partial melting of the lower crust.

5.3 Tectonic setting

5.3.1 Neoproterozoic tectonic setting

The Neoproterozoic magmatism of the Erguna block provides key insights into the convergence and breakup of the Rodinia supercontinent, a significant global geological event, and several magmatic events related to the Rodinia supercontinent breakup have been reported in the Erguna block (Wu et al., 2011; Sun et al., 2012; Tang et al., 2013; Feng, 2015). Magmatisms between 927 Ma and 880 Ma were the result of collision-orogeny during the stage of assembly of the Rodinia supercontinent, whereas the 850–737 Ma magmatisms record the breakup of the Rodinia supercontinent (Zhao, 2017). The study area is located near the Xinlin–Xiguitu suture, and the Neoproterozoic hornblende gneisses of the study area belong to A-type granite, suggesting emplacement in an extensional setting (Figure 5). These gneisses also exhibit characteristics of volcanic-arc granites (Figure 7), indicating their association with the breakup of the Rodinia supercontinent.

5.3.2 Paleozoic tectonic setting

For the Paleozoic era, various tectonic settings have been proposed for the Erguna block. Early Paleozoic igneous rocks in the Erguna block were formed in a post-collision extensional environment, likely linked to the collision and amalgamation of the Erguna and the Xing'an blocks (Feng, 2015; Zhao, 2017). Late Paleozoic granitic magmatism is associated with the collision and assembly of the Erguna–Xing'an and Songnen blocks, transitioning from an orogenic to an extensional environment (Wu et al., 2005; Qian et al., 2018). The collision and assembly between the Erguna block and the Xing'an block were completed in the Early Paleozoic era (Ge et al., 2005), forming collisional accretionary terranes that were accreted during the Late Pan-African global event (Zhou et al., 2011).

The Early Ordovician gabbros show characteristics similar to those of volcanic-arc granites (Figure 7), supporting their connection to the collision and merging of the Erguna and Xing'an blocks. Late Carboniferous–Early Permian intrusive rocks include both A-type and I-type granites, suggesting their emplacement during a transition from orogenic to extensional tectonic settings (Figure 5). These rocks display the characteristics of volcanic-arc and collisional granites (Figure 7), suggesting their emplacement in an orogenic setting. Tectonic activity in the study area during this period was primarily controlled by the collision and amalgamation of the Erguna and Xing'an blocks, followed by the Songnen and Xing'an blocks, which resulted

10.3389/feart.2024.1514658

in the generation of a large amount of intermediate–acidic magmas.

5.3.3 Mesozoic tectonic setting

The Late Permian–Early Jurassic intrusive rocks on the Erguna block were formed in the subduction environment of the MOO plate; the Late Permian–Early Middle Triassic intrusive rocks were formed in the active continental margin environment; the Late Middle Triassic–Early Late Triassic intrusive rocks were formed in a local extensional setting; the Late Triassic–Early Jurassic intrusive rocks were formed in the active continental margin environment; and the Early Jurassic igneous rocks were formed in the active continental margin environment; the Late Jurassic magmatic activity took place in a lithospheric extensional environment caused by the collapse and subsidence of the thickened continental crust after the closure of the Mongolian Okhotsk Ocean (Tang, 2016). The magmatic activity in the Middle Triassic may be related to the extensional environment after the closure of the ancient Asian Ocean; the Early Middle Jurassic magmatic events may be related to the subduction of the MOO (Wang et al., 2012). The Late Triassic intrusive rocks are related to the subduction of the MOO (Liu et al., 2021). The MOO underwent subduction, collision, and post-collision processes during the Early Jurassic to Early Cretaceous, with its closure in the northern part of the Great Xing'an Range likely occurring between the Late Jurassic and Early Cretaceous (Liu et al., 2021). The Early Cretaceous granites were formed in an extensional tectonic setting (Wu et al. ,2009; Shi et al., 2013; Liu et al., 2016) and were related to the final closure of the MOO (Shi et al., 2013; Liu et al., 2016) or the rollback of the Paleo-Pacific Plate (Gao et al., 2013). The geochronological data and tectonic interpretations suggest that the Early Cretaceous intrusive rocks within the study area were formed during non-orogenic extension and were related to the final closure of the MOO or the rollback of the Paleo-Pacific Plate. These intrusive rocks within the study area are distributed in an NE–SW orientation, parallel to the continental margin, and their age decreases from west to east. The intrusive rocks within the Xinlin area yielded a mean age of 125 Ma, which is consistent with the timing of the final closure of the MOO or of the rollback of the Paleo-Pacific Plate. In the discrimination diagram for A-type granites in Figures 5D–F, all the Late Triassic–Early Cretaceous intrusive samples plot within the A-type granite field, suggesting that they formed in an extensional setting.

6 Conclusion

Our study of the tectonic–magmatic activity in the Xinlin area of the Erguna block from the Neoproterozoic to the Mesozoic period leads to the following conclusions:

(1) LA-ICP-MS zircon U–Pb and Muscovite $^{40}Ar/^{39}Ar$ dating suggest that magmatism in the study area occurred during the Neoproterozoic (ca. 864.98 Ma), Early Ordovician (ca. 470.0 Ma), Late Carboniferous (ca. 306.9 Ma), Early Permian (ca. 296.9 Ma), and Early Cretaceous (ca. 117.8 Ma) periods.

(2) The Neoproterozoic and Early Ordovician intermediate–mafic intrusive rocks exhibit low Rb/Sr contents, high $Mg^{\#}$, and weakly negative Eu anomalies. In contrast, the Late Carboniferous, Early Permian, Late Triassic–Early Jurassic, and Early Cretaceous intermediate–acidic intrusive rocks display high Rb/Sr contents, low $Mg^{\#}$, and strongly negative Eu anomalies. These characteristics suggest distinct magma sources: intermediate–acidic magmas were derived from the lower crust, while intermediate–mafic magmas were derived from the mantle and subsequently contaminated by crustal material.

(3) Neoproterozoic intrusive rocks in the Xinlin area formed during the breakup of the Rodinia supercontinent. Paleozoic intrusive rocks were formed during the collision and amalgamation of the Erguna, Xing'an, and Songnen blocks. Early Mesozoic intrusive rocks were associated with the subduction of the Mongol-Okhotsk oceanic intracontinental system, while Late Mesozoic intrusive rocks developed in a non-orogenic extensional tectonic setting, linked to either the final closure of the MOO or the rollback of the Paleo-Pacific Plate.

Data availability statement

The original contributions presented in the study are included in the article/supplementary material; further inquiries can be directed to the corresponding author.

Author contributions

SL: data curation, formal analysis, software, and writing–original draft. CL: data curation and writing–review and editing. MA: methodology and writing–review and editing. ZS: software and writing–review and editing. XZ: formal analysis and writing–review and editing. AF: methodology and writing–review and editing. WY: methodology and writing–review and editing.

Funding

The author(s) declare that financial support was received for the research, authorship, and/or publication of this article. This work was financially supported by the Key Research and Development Project of Heilongjiang Province (GA21A204 and HKY202401).

Acknowledgments

The authors are grateful to professor Yang Liu for his kind help during the field work and professor Keyong Wang for his guidance in preparing this manuscript.

Conflict of interest

The authors declare that the research was conducted in the absence of any commercial or financial relationships that could be construed as a potential conflict of interest.

Generative AI statement

The author(s) declare that no generative AI was used in the creation of this manuscript.

Publisher's note

All claims expressed in this article are solely those of the authors and do not necessarily represent those of their affiliated organizations, or those of the publisher, the editors and the reviewers. Any product that may be evaluated in this article, or claim that may be made by its manufacturer, is not guaranteed or endorsed by the publisher.

Supplementary material

The Supplementary Material for this article can be found online at: https://www.frontiersin.org/articles/10.3389/feart.2025.1514658/full#supplementary-material

References

Andersen, T. (2002). Correction of common lead in U–Pb analyses that do not report ^{204}Pb. *Chem. Geol.* 192, 59–79. doi:10.1016/s0009-2541(02)00195-x

Boynton, W. V. (1984). "Geochemistry of the rare earth elements: meteor-ite studies," in *Rare earth element geochemistry*. Editor P. Henderson (New York: Elservier), 63–114.

Chai, M. C., Wang, Q., Zhao, G. Y., Gao, S., and Cao, K. (2018). Zircon U-Pb ages and geochemical characteristics of Late Mesozoic volcanic rocks from Shibazhan-Hanjiayanzi area of Da Hinggan Mountains and their tectonic significance. *Geol. Bull. China* 37 (10), 1866–1881. (in Chinese with English abstract). doi:10.16509/j.georeview.2018.03.004

Chen, W., Zhang, W., Zhang, Y. Q., Jin, G. S., and &Wang, Q. L. (2006). Late Cenozoic episodic uplifting in southeastern part of the Tibetan plateau-evidence from Ar-Ar thermochronology. *Acta Petrol. Sin.* 22 (4), 867–872. (in Chinese with English abstract).

Dai, H. M., Yang, Z. F., Ma, Z. D., and Gong, C. D. (2013). The petrogeochemical characteristics and tectonic setting of Mesozoic intrusive rocks in Chabaqi area of the Da Hinggan Mountains. *Geol. China* 40 (1), 232–247. (in Chinese with English abstract).

Ewart, A., Milner, S. C., Armstrong, R. A., and Dungan, A. R. (1998). Etendeka volcanism of the goboboseb mountains and messum igneous complex, Namibia. Part I: geochemical evidence of early cretaceous tristan plume melts and the role of crustal contamination in the parana-etendeka CFB. *J. Petrology* 39 (2), 191–225. doi:10.1093/petroj/39.2.191

Feng, Z. Q. (2015). The Palezoic tectono-magmatic evolution of the northern Great Xing'an range. *M.Phil. Diss. Jilin Univ.* (in Chinese with English abstract).

Feng, Z. Q., Liu, Y. J., Wen, Q. B., Han, G. Q., Li, W. M., and Zhang, L. (2014). Petrogenesis of ~330 Ma meta-gabbro-granite from the Tayuan area in the northern segment of the Da Xing'an Mts and its tectonic implication. *Acta Petrol. Sin.* 30 (7), 1982–1994. (in Chinese with English abstract).

Frost, B. R., Barnes, C. G., Collins, W. J., Arculus, R. J., Ellis, D. J., and Frost, C. D. (2001). A geochemical classification for granitic rocks. *J. Petrol* 42, 2033–2048. doi:10.1093/petrology/42.11.2033

Gao, Y., Zheng, C. Q., Yao, W. G., Wang, H., Li, J., Shi, L., et al. (2013). Geochemistry and Ziron U-Pb geochronlogy of the Luotuobozi pluton in the Haduohe area in the northern DaXing'anling. *Acta Geol. Sin.* 87 (9), 1293–1310. (in Chinese with English abstract).

Ge, W. C., Chen, J. S., Yang, H., Zhao, G. C., Zhang, Y. L., and Tian, D. X. (2015). Tectonic implications of new zircon U–Pb ages for the Xinghuadukou complex, Erguna massif, northern Great Xing'an range, NE China. *J. Asian Earth Sci.* 106, 169–185. doi:10.1016/j.jseaes.2015.03.011

Ge, W. C., Wu, F. Y., Zhou, C. Y., and Abdel Rahman, &A. A. (2005). The age of Tahe granite in the northern Daxing'an mountains and its constraints on the structural attribution of the Erguna block. *Sci. Bull.* 50 (12), 1239–1247. (in Chinese with English abstract).

Guo, Y. F., Yang, Y. C., Han, S. J., Tan, Y., and &Bo, J. W. (2016). Geochemistry and zircon U Pb dating of the tonalite from fenghuangshan area in daxing'anling. *J. Univ. (Earth Sci. Edtion)* 46 (5), 1406–1417. (in Chinese with English abstract). doi:10.13278/j.cnki.jjuese.201605111

HBGMR (Heilongjiang Bureau of Geology and Mineral Resources) (1997). *Rock stratigraphic units*. Wuhan: China university of Geoscience Press. (in Chinese with English abstract).

Hu, X. L., Yao, S. Z., He, M. C., Ding, Z. J., Liu, M., Cui, Y. B., et al. (2014). Sulfur and lead isotopic characteristics of Chalukou and Daheishan porphyry Mo deposits in northern segment of Da Hinggan Mountains. *Mineral. Deposits* 33 (4), 776–784. (in Chinese with English abstract). doi:10.16111/j.0258-7106.2014.04.027

Irvine, T. H., and Baragar, W. R. A. (1971). A guide to the chemical classifica-tion of the common volcanic rocks. *Can. J. Earth Sci.* 8 (5), 523–548. doi:10.1139/e71-055

Jahn, B. M. (2004). *The central asian orogenic belt and growth of the continental crust in the phanerozoic*. Geological Society, London, Special Publications, 226 (1), 73–100.

Jia, P. P., Wei, J. H., Gong, Q. W., and Zhao, W. L. (2011). Analysis of geolog-ical background and ore-searching prospect for copper-molybdenum deposits in the Da Hingan Ling area. *Geol. Explor.* 47 (2), 0151–0162. (in Chinese with English abstract).

Ju, W. X., Su, S. J., Bai, C. X., and Shao, J. (2005). Charateristics of the late carboniferous banlashan series of intrusive rock in orqohan area, dahingganling. *Geol. Resour.* 14 (3), 161–165. (in Chinese with English abstract).

Lightfoot, P. C., Hawkesworth, C. J., and Sethna, S. F. (1987). Petrogenesis of rhyolites and trachytes from the Deccan Trap: Sr, Nd and Pb isotope and trace element evidence. *Contributions Mineralogy Petrology* 95 (1), 44–54. doi:10.1007/bf00518029

Liu, B. B., Wang, J. G., Bai, C. D., Zhang, X. Q., Li, D., Zhang, Z. X., et al. (2021). Zircon U-Pb geochronology, geochemistry and geological significance of late triassic and early cretaceous granites in aduta area, northern daxing'an mountains. *Hebeidizhidaxuexuebao* 44 (2), 8–18. (in Chinese with Englishabstract). doi:10.13937/j.cnki.hbdzdxxb.2021.02.002

Liu, J., Liu, Z. H., Li, S. C., Zhao, C., Wang, C. J., Peng, Y. B., et al. (2016). Geochronology and geochemistry of Triassic intrusive rocks in Kaiyuan area of the eastern section of the northern margin of North China. *Acta Petrol. Sin.* 32 (9), 2739–2756. (in Chinese with English abstract).

Liu, J. L., Bai, X. D., Zhao, S. J., Tran, M. D., Zhang, Z. C., Zhao, Z. D., et al. (2011). Geology of the Sandaowanzi telluride gold deposit of the northern GreatXing'an Range, NE China: geochronology and tectonic controls. *J. Asian Earth Sci.* 41, 107–118. doi:10.1016/j.jseaes.2010.12.011

Liu, Y. F., Jiang, S. H., and &Zhang, Y. (2010). The SHRIMP zircon U-Pb dating and geological features of Bairendaba diorite in the Xilin-haote area, Inner Mongolia, China. *Geol. Bull. China* 29 (5), 688–696. (in Chinese with English abstract).

Liu, Y. J., Li, W. M., Feng, Z. Q., Wen, Q. B., Franz, N., and &Liang, C. Y. (2017). A review of the paleozoic tectonics in the eastern part of central asian orogenic belt. *Gondwana Res.* 43, 123–148. doi:10.1016/j.gr.2016.03.013

Lu, S. (2019). *Metallogenic regularities and metallogenic prognosis of gold deposits in Xinlin- han jia Yuan area, Great Xing'an range, China M.Phil.* Jilin University. (in Chinese with English abstract).

Lu, S., Deng, C. Z., Wang, K. Y., Feng, Y. Z., Li, C. L., Chen, J. Y., et al. (2022). Crustal contribution for the formation of the Walali Au deposit and implications on the early cretaceous Au mineralization in the northern Great xing'an range. *Ore Geol. Rev.* 147 (2022), 105000. doi:10.1016/j.oregeorev.2022.105000

Lu, S., Wang, K. Y., Liu, Y., Deng, C. Z., and Jing, B. Y. (2020). Geochronological and geochemical data for Late Palaeozoic–Mesozoic intrusive rocks in the Wenkutu area, northeastern China: new constraints on the tectonic evolution of the Great Xing'an Range. *Geol. J.* 55, 1357–1379. doi:10.1002/gj.3494

Ludwig, K. R. (2003). *Isoplot 3.00: a geochronological toolkit for microsoft excel.* California, Berkeley: Berkeley Geochronology Center, 39.

Maniar, P. D., and Piccoli, P. M. (1989). Tectonic discrimination of granitoids. *Geol. Soc. Am. Bull.* 101, 635–643. doi:10.1130/0016-7606(1989)101<0635:tdog>2.3.co;2

Miao, L. C., Fan, W. M., Zhang, F. Q., Liu, D. Y., Jian, P., Shi, G. H., et al. (2004). Zircon SHRIMP geochronology of the Xinkailing-Kele complex in the northwestern Lesser Xing'an Range, and its geological implications. *Chin. Sci. Bull.* 49, 201–209. doi:10.1360/03wd0316

Niu, Y. H., Liu, Y., Zhou, Z. G., Niu, W. Z., Liu, C. F., Zhao, X. Q., et al. (2016). Chronology,geochemistry and geological significance of the Early Cretaceous intrusive rocks from the Tahe region,northeastern China. *Sediment. Geol. Tethyan Geol.* 36 (4), 95–105. (in Chinese withEnglish abstract).

Ouyang, H. G., Mao, J. W., Zhou, Z. H., and Su, H. M. (2015). Late mesozoic metallogeny and intracontinental magmatism, southern Great Xing'an range, northeastern China. *Gondwana Res.* 27, 1153–1172. doi:10.1016/j.gr.2014.08.010

Peasrce, J. A., Harris, N. B. W., and &Tindle, A. G. (1984). Trace element discrimination diagrams for the tectonic interpretation of granitic rocks. *J. Petrology* 25 (4), 956–983. doi:10.1093/petrology/25.4.956

Peccerillo, A., and Taylor, A. R. (1976). Geochemistry of Eocene calc-alkaline volcanic rocks from the Kastamonu area, Northern Turkey. *Contribu-tions Mineralogy Petrology* 58, 63–81. doi:10.1007/bf00384745

Qian, C., Lu, L., Qin, T., Li, L. C., Chen, H. J., Cui, T. R., et al. (2018). The early late-Paleozoic granitic magmatism in the Zalantun region, northern Great Xing'an range, NE China: constraintson the timing of amalgamation of erguna-Xing'an and Songen blocks. *Acta Geol. Sin.* 92 (11), 2190–2214. (in Chinese with Englishabstract).

Shao, J. A., and Mu, B. L. (1999). Magmatism in the mesozoic extending orogenic process of da Hinggan MTS. *Earth Sci. Front.* 6 (4), 339–346. (in Chinese withEnglish abstract).

Shi, L., Zheng, C. Q., Yao, W. G., Li, J., Xu, J. L., Gao, Y., et al. (2013). Geochronology, petro-geochemistry and tectonic setting of the hamagou forest farm A-type granites in the wuchagou region, central Great xinggan range. *Acta Geol. Sin.* 87 (9), 1264–1276. (in Chinese with English abstract).

Steiger, R. H., and Jager, E. (1977). Subcommission on geochronology:convention on the use of decay constants in geo- and cosmochronology. *Earth Planet. Sci. Lett.* 36, 359–362. doi:10.1016/0012-821x(77)90060-7

Sui, Z. M., Ge, W. C., Wu, F. Y., Zhang, J. H., Xu, X. C., and Cheng, R. Y. (2007). U-Pb ages,geochemistry and its petrogenesis of Jurassic granites in northeastern part of the Da Hinggan Mts. *Acta Petrol. Sin.* 23 (2), 461–480. (in Chinese withEnglish abstract).

Sun, L. X., Ren, B. F., Zhao, F. Q., and Peng, L. N. (2012). Zircon U-Pb ages and Hf isotope characterstics of Taipingchuan large porphyritic granite pluton of Erguna Massif in the Great Xing'an Range. *Earth Sci. Front.* 19 (5), 114–122. (in Chinese with English abstract).

Sun, S. S., and McDonough, W. F. (1989). "Chemical and isotopic systematics of oceanic basalts: implications for mantle composition and processes,". *Magmatism in ocean basins*. Editors A. D. Saunders, and M. J. Norry (London: Geological Society Special Publication), 42, 313–345. doi:10.1144/gsl.sp.1989.042.01.19

Tang, J. (2016). Geochronology and geochemistry of the Mesozoic igneous rocks in the Erguna Massif, NE China: constraints on the tectonic evolution of the Mongol-Okhotsk suture zone. *M.Phil. Diss. Jilin Univ.* (in Chinese with English abstract).

Tang, J., Xu, W. L., Wang, F., Wang, W., Xu, M. J., and Zhang, Y. H. (2014). Geochronology and geochemistry of early–middle triassic magmatism in the Erguna massif, NE China: constraints on the tectonic evolution of the mongol–okhotsk ocean. *Lithos* 184-187, 1–16. doi:10.1016/j.lithos.2013.10.024

Tang, J., Xu, W. L., Wang, F., Xu, M. J., and Zhang, Y. H. (2013). Geochronology and geochemistry of neoproterozoic magmatismin the Erguna massif,NE China: petrogenesis and implications for the breakup of the Rodinia supercontinent. *Precambrian Res.* 224, 597–611. doi:10.1016/j.precamres.2012.10.019

Wang, F. L., Wang, H. P., Lu, H. F., Yu, H. F., Chen, Y., Yang, H., et al. (2016). Geochronology, petrogeochemical characteristics and tectonic setting of Mesozoic granite in Shangqi area of the Da Hinggan Mountains. *Geol. Sci. Technol. Inf.* 35 (4), 18–28. (in Chinese with English abstract).

Wang, W., Xu, W. L., Wang, F., and &Meng, E. (2012). Zircon U-Pb chronology and assemblages of mesozoic granitoids in the manzhouli-erguna area, NE China: constraints on the regional tectonic evolution. *Geol. J. China Univ.* 18 (1), 88–105. (in Chinese with Englishabstract). doi:10.16108/j.issn1006-7493.2012.01.010

Whalen, J. B., Currie, K. L., and Chappell, B. W. (1987). A-type granites: geochemical characteristics, discrimination and petrogenesis. *Contrib. Mineral. petr* 95, 407–419. doi:10.1007/bf00402202

Wu, F. Y., Sun, D. Y., Ge, W. C., Zhang, Y. B., Grant, M. L., Wilde, S. A., et al. (2011). Geochronology of the Phanerozoic granitoids in northeastern China. *J. Asian Earth Sci.* 41, 1–30. doi:10.1016/j.jseaes.2010.11.014

Wu, G. (2006). Metallogenic setting and metallogenesis of nonferrous -precious metals in northern da Hinggan moutain. *M.Phil. Diss. Jilin Univ.* (in Chinese with English abstract).

Wu, G., Chen, Y. J., Sun, F. Y., Li, J. C., Li, Z. T., and Wang, X. J. (2008). Geochemistry of the Late Jurassic granitoids in the northern end area of Da Hinggan Mountains and their geological and prospecting implications. *Acta Petrol. Sin.* 24 (4), 899–910. (in Chinese with English abstract).

Wu, G., Chen, Y. J., Zhao, Z. H., Zhao, T. P., Li, Z. T., and Zhang, Z. (2009). Geochemistry, zircon SHRIMP U-Pb age and petrogenesis of the east luoguhe granites at the northern end of the Great hinggan range. *Acta Petrol. Sin.* 25 (2), 233–247.

Wu, G., Sun, F. Y., Zhao, C. S., Li, Z. T., Zhao, A. L., Pang, Q. B., et al. (2005). Discovery and geological significance of early paleozoic post collisional granites on the northern edge of the Erguna block. *Sci. Bull.* 50 (20), 2278–2288. (in Chinese with English abstract).

Xu, W. L., Pei, F. P., Wang, F., Meng, E., Ji, W. Q., Yang, D. B., et al. (2013). Spatial-temporal relationships of Mesozoic volcanic rocks in NE China: constraints on tectonic overprinting and transformations between multiple tectonic regimes. *J. Asian Earth Sci.* 74, 167–193. doi:10.1016/j.jseaes.2013.04.003

Yang, H. B., Liu, Y., Zheng, J. L., Liang, Z. K., Wang, X. Y., Tang, X. F., et al. (2017). Petrogenesis and geological significance of Neopro•terozoic amphibolite and granite in Bowuleshan area, Erguna massif, Northeast China. *Geol. Bull. China* 36 (2/3), 342–356. (in Chinese with English abstract).

Zhang, Y., Chen, W., Chen, K. L., and &Liu, X. Y. (2006). Study on the Ar-Ar age spectrum of diagenetic I/S and the mechanism of ^{39}Ar recoil loss-examples from the clay minerals of P-T boundary in changxing, Zhejiang Province. *Geol. Rev.* 52 (4), 556–561. (in Chinese with English abstract).

Zhang, Y. L., Ge, W. C., Liu, X. M., and Zhang, J. H. (2008). Isotopic characteristics and their significance of the Xinlinzhen pluton, Great Hinggan mountains. *J. Jilin Univ. Earth Sci.* 38, 177–186. (in Chinese with English abstract). doi:10.1109/tmag.2018.2845903

Zhao, S., (2017). Neoproterozoic-Early Paleozoic tectonic evolution and attribute of the Erguna Massif: constraints from detrital zircon U-Pb geochronology and igneous rock associations. M.Phil. Dissertation of Jilin University (in Chinese with English abstract).

Zhao, S., Xu, W. L., Wang, F., Wang, W., Tang, J., and &Zhang, Y. H. (2016). Neoproterozoic magmatisms in the Erguna massif, NE China: evidence from zircon U-Pb geochronology. *Geotect. Metallogenia* 40 (3), 559–573. (in Chinese with English abstract). doi:10.16539/j.ddgzyckx.2016.03.012

Zheng, J. L., Zhang, W. Q., and Xu, L. M. (2015). Geochemistry characteristics and metallogenic prognosis of the volcanic rocks from Manitu Forma-tion of Bowule mountain area in Da Hinggan mountain. *GoldScience Technol.* 23 (1), 46–52. (in Chinese with English abstract). doi:10.11872/j.issn.1005-2518.2015.01.046

Zhou, J. B., Wilde, S. A., Zhang, X. Z., Ren, S. M., and Zheng, C. Q. (2011). Early Paleozoic metamorphic rocks of the Erguna block in the Great Xing'an Range, NE China: evidence for the timing of magmatic and metamorphic events and their tectonic implications. *Tectonophysics* 499, 105–117. doi:10.1016/j.tecto.2010.12.009